EMBRY-RIDDLE
Aeronautical University™
SCHOLARLY COMMONS

12-3-2014

Proof of Concept Test for Dual-Axis Resonant Phase-Locked Excitation (PhLEX) Fatigue Testing Method for Wind Turbine Blades

Jenna Austin Beckwith

Follow this and additional works at: https://commons.erau.edu/edt

Proof of Concept Test for Dual-Axis Resonant Phase-Locked Excitation (PhLEX) Fatigue Testing Method for Wind Turbine Blades

Jenna Austin Beckwith

Master of Science in Mechanical Engineering

December 3, 2014

Embry-Riddle Aeronautical University

600 S. Clyde Morris Blvd.

Daytona Beach, FL 32114

Proof of Concept Test for Dual-Axis Resonant Phase -Locked Excitation (PhLEX) Fatigue Testing Method for Wind Turbine Blades

by

Jenna Austin Beckwith

This thesis was prepared under the direction of the candidate's thesis committee chairman, Dr. Darris White, Department of Mechanical Engineering, and has been approved by the members of his/her thesis committee. It was submitted to the Mechanical Engineering Department and was accepted in partial fulfillment of the requirements for the degree of Master of Science in Mechanical Engineering.

Thesis Review Committee:

Darris White, Ph. D.
Committee Chair

Charles Reinholtz, Ph. D.
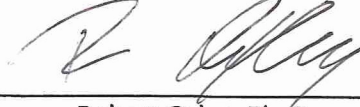Committee Member

Marc Compere, Ph. D.
Committee Member

Michael Desmond
Committee Member

Jean-Michel Dhainaut, Ph. D.
Graduate Program Chair,
Mechanical Engineering

Charles Reinholtz, Ph. D.
Department Chair,
Mechanical Engineering

Maj Mirmirani, Ph. D.
Dean,
College of Engineering

Robert Oxley, Ph. D.
Associate Vice President of
Academics

12-9-14

ABSTRACT

TITLE: Proof of Concept Test for Dual-Axis Resonant Phase-Locked Excitation (PhLEX) Fatigue Testing Method for Wind Turbine Blades

CANDIDATE: Jenna Austin Beckwith

DEGREE: Master of Science in Mechanical Engineering

INSTITUTION: Embry-Riddle Aeronautical University

YEAR: 2014

The installed capacity of wind turbines has grown steadly for the past decade with wind energy now providing 3.6-percent of the U.S.'s electricity supply [13]. This trend can be attributed to advancements in wind turbine technology and the ability to increase wind turbine sizes. As wind turbines grow in size, so do the loads experienced by the turbine. One of the most significant load increases is in the lead-lag direction of the wind turbine blades. The increase in lead-lag load is due to the increase in weight of the larger blades. Current wind turbine blades have lead-lag and flapwise loads on the same order of magnitude. The blades of wind turbines are critical components, and full-scale blade fatigue testing is a necessary step to validate blade designs. A collaborative effort between the National Renewable Energy Laboratory (NREL) and Embry-Riddle Aeronautical University (ERAU) has resulted in the development of the dual-axis resonant Phase-Locked Excitation (PhLEX) fatigue test method. The PhLEX method fatigues wind turbine

blades by loading both flapwise and lead-lag directions simultaneously at the lead-lag fundamental frequency while controlling the phase between the directional loadings. The PhLEX method offers a load distribution that accurately resembles field operation loads while decreasing test duration. A proof-of-concept test of the PhLEX method was conducted at the National Wind Technology Center (NWTC) in July of 2012. It was found that a dual-axis resonant test running at the lead-lag fundamental frequency could be run in a controlled manner, with both the lead-lag and flapwise directions demonstrating first mode deflections. The PhLEX proof-of-concept test set-up and the results and conclusions of the proof-of-concept test are presented in this thesis.

TABLE OF CONTENTS

TABLE OF FIGURES

TABLE OF TABLES

LIST OF ACRONYMS

BETS	Base Excitation Test System
B-REX	Blade Resonance EXcitation
DC	Direct Current
E	Modulus of Elasticity
ERAU	Embry-Riddle Aeronautical University
FEM	Finite Element Model
GJ	Giga-Joules
GW	Giga-Watts
HAWT	Horizontal-Axis Wind Turbine
hp	horsepower
HP	High-Pressure
hr	hour
Hz	Hertz
I	Moment of Inertia
IEC	International Electrotechnical Commission
IREX	Inertial Resonance EXcitation
kN	kilo-Newton
kW	kilo-Watts
LP	Low-Pressure
LVDT	Linear Variable Differential Transducer
m	meter
mm	millimeters
MPL	mass-per-length
MRAC	Model Reference Adaptive Controller
MW	Mega-Watts
NAREC	NAtional Renewable Energy Center
NREL	National Renewable Energy Laboratory
NWTC	National Wind Technology Center
PhLEX	Phase-Locked EXcitation
PID	Proportional-Integral-Derivative
s	second
SNL	Sandia National Laboratory
UREX	Universal Resonant EXcitation

CHAPTER 1: INTRODUCTION TO WIND TURBINES

The wind turbine has become an icon for clean energy. The three-bladed horizontal axis wind turbines that are used to represent the movement towards clean energy are marvels of modern engineering. These turbines utilize composite materials and advanced control systems to increase the power output while decreasing their cost. While using wind to produce electricity on an industrial scale is relatively new, using wind as a power source is an old technology.

1.1   Historical Review of Wind Machines

The first instance of a wind powered machine comes from the 1st century AD. Hero of Alexandria describes in his work *Pneumatica*, a toy organ that has its bellows powered by a windmill [1-3].

The next recorded reference to a wind-powered machine is in 644. A story is told of a Persian man that claims to build mills powered by wind [1-3]; however, a detailed description of a windmill is not seen in Persia until the fourteenth century [2]. The description of the Persian windmills comes from a region called Seistan, modern day eastern Iran, that is known for its consistent, high wind speeds [2, 3]. The Persian windmills had a vertical drive shaft that had sails mounted radially around it. These components made up the rotor of the windmill [1, 2].

Windmills appeared in England and France during the 12th century. Early European windmills were typically post mills, so called because the rotor and drive train were

set on a large vertical post to control the yaw of the rotor. Post mills are horizontal axis machines driven by lift forces, whereas the Persian windmills were vertical axis machines driven by drag forces [3-5]. The transformation from a vertical-axis wind mill to a horizontal-axis windmill is largely undocumented, but it is speculated that it followed the development of rigging on ships [3]. Windmills continued to develop as power demands grew. In the 18th and 19th centuries smock mills or tower mills, began to replace post mills due to their ability to hold larger rotors. [5, 6].

When the Americas were colonized during the 17th and 18th centuries, the wind mill was widely used in saw mills and grain mills. There was not significant development until the mid-West began to be settled. The land in the mid-west is semi-arid, with the majority of the water in aquifers. Wind powered well pumps were a convenient way to get at the underground water. The low-speed, high-torque application and a need to be self-regulating drove several advancements in the American wind machine. Americans experimented with varying solidities, the ratio of the swept area of the wind machine rotor and the area occupied by sails, or blades. [5, 7].

Wind mills began to be developed as electricity producing machines in the 1880's, following the appearance of electric generators. These machines started as small installations. Wind turbines were not used for large electricity generating until 1939. Small wind turbines were developed with increasing interest from the public during the war years of World War I and World War II due to scarcity of fuel from regular suppliers. In the post-war years, wind turbines were mostly forgotten due to

the availability of coal and oil. In was not until the oil crisis of 1973 that wind turbines were considered on a commercial scale again [3, 8, 9].

Interest in wind power has been reignited in recent years due to concerns about the environment, the finite amount of fossil fuels, and political reasons. With the wind industry following the example of other large industries such as aerospace and automotive, new materials and manufacturing techniques have led to the rapid advancement of wind turbines to the large structures we recognize today [8, 9].

1.2   Modern Wind Industry

1.2.1   Industry Growth

The global installed capacity of wind power at the end 2013 was 318-GW. From 2002 to 2012, installed wind power had grown annually by 24-percent. In 2013, the growth rate dropped to 13-percent. This is in part due to the large amount of wind power being installed at the end of 2013; in the United States alone, 12-GW was under construction in December of 2013. This will also affect annual growth of 2014, boosting the growth rate to a predicted 34-percent [10, 11]. Projections expect current trends to continue [12].
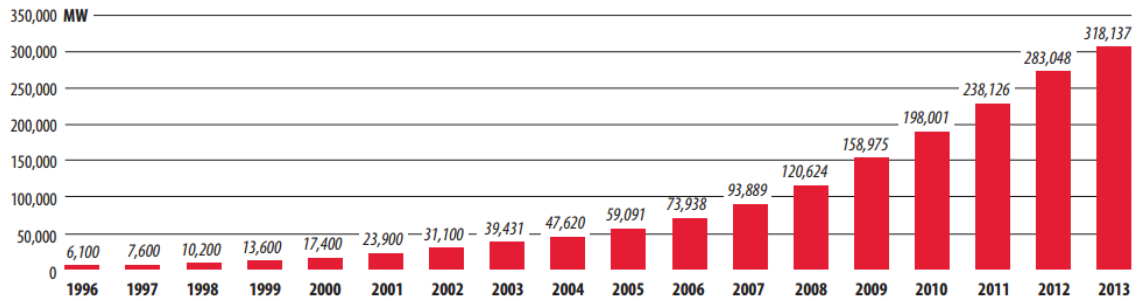
Figure 1.1: Global Cumulative Installed Wind Capacity 1996 to 2013 [10]
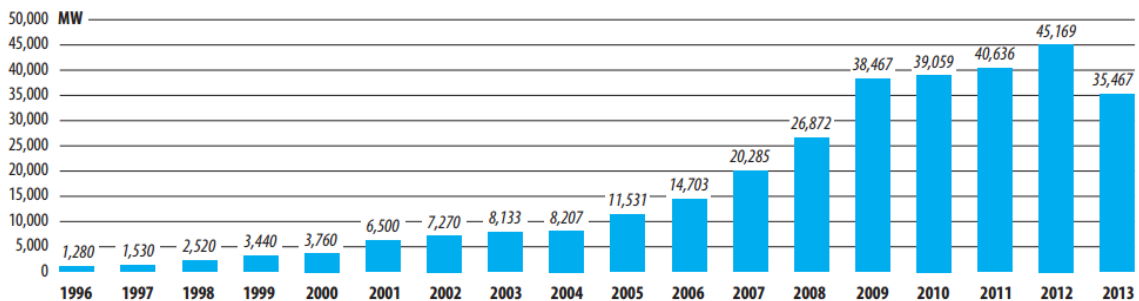
Figure 1:2: Global Annual Installed Wind Capacity 1996 to 2013 [10]

1.2.2 Cost of Energy

Wind power is now second highest renewable energy contributor, behind hydro power, providing 3.6-percent of United States electricity [13]. The price of wind energy has dropped from 55 cents per kW·hr in 1980 to less than six cents in 2014 [13].

1.2.3 Cost of Investment

The investment cost of wind power is becoming competitive with other methods of electricity generation. Onshore wind installations average at 2000-USD/kW, and offshore installations average at 4500-USD/kW. Onshore installations are already

14

similarly priced to coal plants, 1800-USD/kW, and are approaching natural gas plants, 750-USD/kW [11]. Offshore wind installations are higher due to the logistics of installation and power; however, significant research is going into offshore wind power and the investment costs are expected to decrease by 23-percent by 2020 [11]. Reductions in investment cost of onshore installations are also predicted, but at a more modest rate of 12-percent [11].

1.2.4 The Modern Wind Turbine

The most common modern wind turbine is the upwind, horizontal axis wind turbine (HAWT) [3, 11, 14]. These machines utilize three, evenly spaced blades, pitch regulation, and variable speed generation. While there are various wind turbine configurations still widely used, the HAWT is most common for large-scale electricity generation [12].

A land-based HAWT can be broken down into six primary systems: the rotor, the drivetrain, the nacelle, the tower, the controls, and the electrical system [3]. These sub-systems are shown in Figure 1.3.
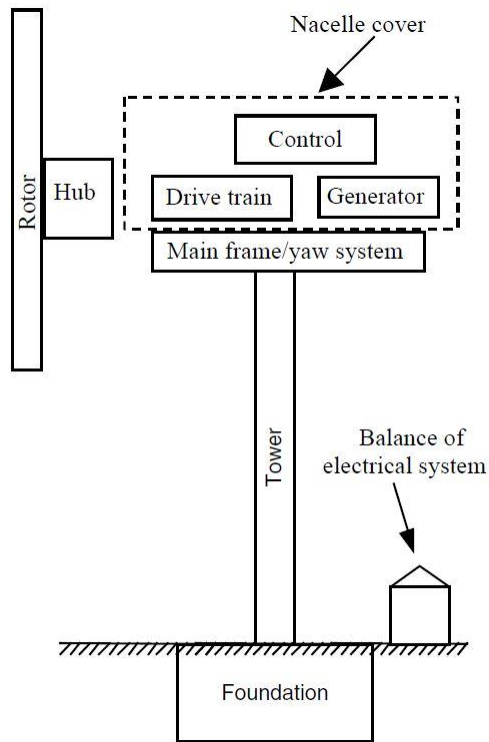
Figure 1.3: Modern HAWT Components [3]

The rotor consists of the hub and the blades. Wind turbine blades are generally

considered the most important component of a wind turbine [3, 14-16]. The

importance of the blades is due to the effect they have on the performance and cost

of the turbine. In order to improve performance and reduce costs of blades, new

blade designs are being developed that use longer blades and advanced materials.

The biggest design change of turbine blades is the increasing length. The power

output of a wind turbine is directly proportional to the swept area of the rotor [17-

19]. In order to increase power output, wind turbines have been increasing in size.

The size of HAWTs has doubled from 2002 to 2012, as can be seen in Figure 1.4. It is

expected that by 2016, the average blade length will be 50-meters [12].

16
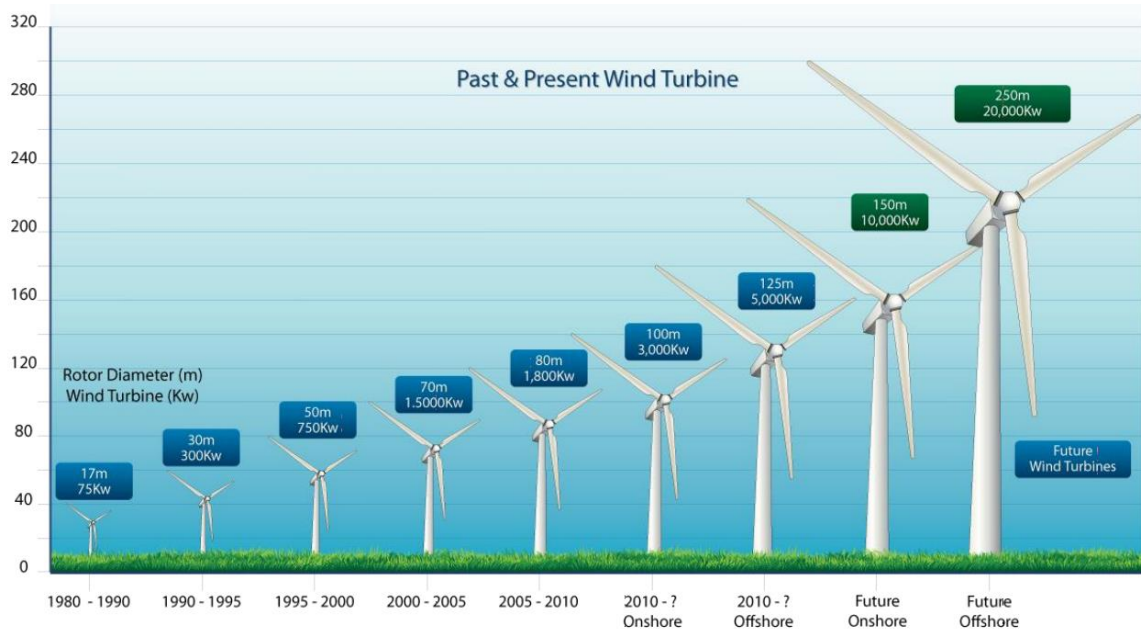
Figure 1.4: Wind Turbine Rotor Size from 1980 to 2010 with Future Speculation [11]

As wind turbine blades grow in length, so do the loads imparted on them. In order to ensure blade performance, new blade designs are tested extensively. Simulations of blade performance are conducted throughout the design process. Due to the complex structure of blades, simulation alone is not sufficient to validate blade performance. Full-scale blade testing is used to verify blade design and demonstrate blade performance [15].

1.3   Wind Turbine Blade Properties

1.3.1   Blade Nomenclature

For the purpose of this paper, the three principle directions of a wind turbine blade are flapwise, lead-lag, and spanwise. These directions, shown in Figure 1.5, are

mutually orthogonal to each other, and do not vary along the length of the

blade [16].
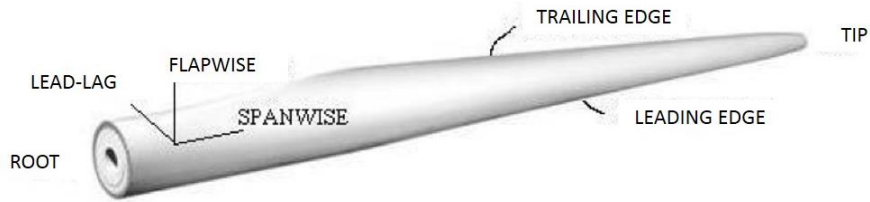
Figure 1.5: Principle Direction of Wind Turbine Blade [20]

Wind turbine blades use airfoils to convert kinetic energy in the wind to rotational

energy about the generator shaft. A typical airfoil cross-section is shown in

Figure 1.6 in which the lead-lag, designated as x, and the flapwise, designated as y,

directions are normalized over the chord length.
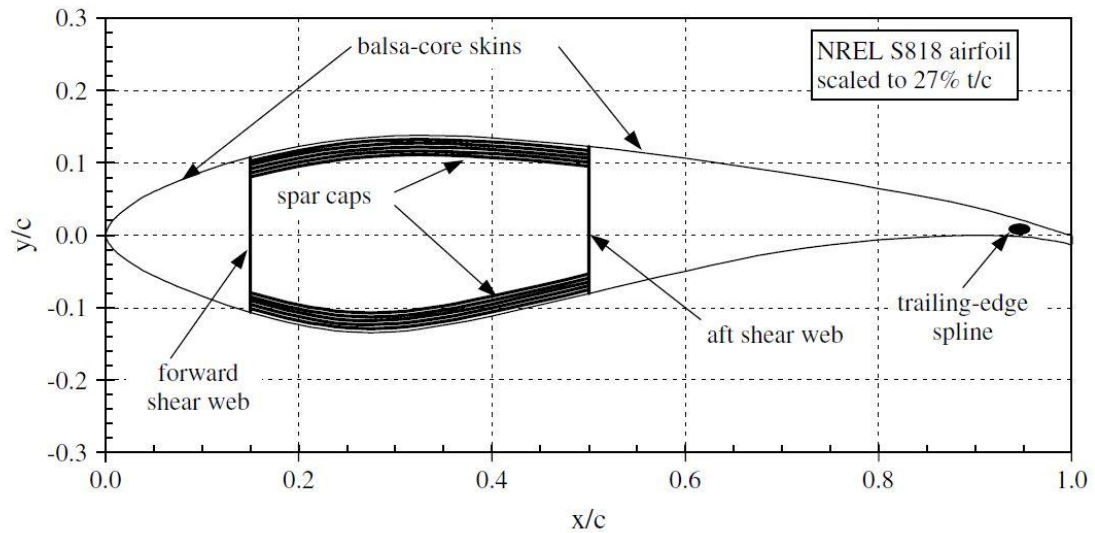
Figure 1.6: Typical Airfoil Cross-Section Normalized Over Chord Length [14]

The leading edge is the point on the airfoil where the wind first contacts the profile. The trailing edge is on the opposite end of the airfoil. The line that connects the leading edge and the trailing edge of an airfoil is called the chord [16, 18, 21]. An airfoil generates lift by creating a low-pressure area on one side of the airfoil and a high-pressure area on the other side. The low-pressure (LP) surface is on the convex side of the profile, making the concave side the high-pressure (HP) surface [21].

1.3.2   Blade Geometry

A wind turbine blade connects to the hub at the root of the blade. The root of large turbine blades typically have a circular cross-section to interface with the hub. The circular cross-section of the root transitions into an airfoil cross-section at the lift-generating portion of the blade [16, 17]. The transition region of a blade has complex dynamics and is prone to high stresses [15].

The airfoil cross-section of a wind turbine blade is not constant along the length of the blade. It is common to use multiple airfoils along the length of the blade that are most efficient for the relative wind speeds seen at that section of the blade. The transition between airfoils is a gradual transition, unlike the transition from root to lift-generating region [21].

The chord of each airfoil along the spanwise direction is angled relative to the chords of the airfoils surrounding it. This is to have an optimal angle of attack along the blade. This is called the twist of the blade [21]. The length of the chord also varies along the spanwise direction, decreasing toward the tip [21]. Due the

decreased chord and smaller amount of material used along the blade, the mass of the blade decreases along the spanwise direction from root to tip [21].

1.3.3 Materials and Manufacture of Blades

The trend of increasing the rotor radius of wind turbine blades to increase power output is demanding the materials and manufacturing process be re-evaluated [10]. Typical wind turbine blades use fiberglass and balsa wood or foam [14, 22]. These materials have a higher strength to weight ratio than earlier materials used for blades, such as hard woods and metals, but fiberglass composites are reaching the limit of their utility for current blade lengths [10, 14]. New materials such as carbon fiber are being investigated to replace fiberglass as stronger, lighter substitutes; however the cost of these materials have not yet made it economical to move away from fiberglass [14].

A typical blade cross-section is shown in Figure 1.6. The airfoil shape, or the skin, of the blade is a laminate structure using multi-axial fiberglass with a balsa wood or foam core [14]. The skin is made in two pieces that are joined at the leading and trailing edges. The most common method for creating the complex curvature of the skin is hand lay-up of an open mold. The spar caps and the shear webs are the load carrying structures of the wind turbine blade. The spar cars and shear webs are thick laminates with primarily unidirectional fibers [14, 22].

Hand lay-up is a method prone to defects due to the many variables that come with having a human operator. Joining the skins and the shear webs can also introduce

flaws. More controlled methods of blade construction are being investigated, including pre-impregnated fibers, transfer molding, and spindle fibers [22]. As materials and methods of fabrication are developed, testing is required to validate new designs.

1.4   Wind Turbine Blade Loads

1.4.1   Aerodynamic Loads

Wind turbine blades are subjected to two primary loads: aerodynamic loads and inertial loads [15, 23]. Aerodynamic loads consist of drag and lift forces caused by the interaction of the blades with the wind. Wind has both stochastic and deterministic components. The deterministic component is a steady load that increases with height. The variance with height is a direct result of the boundary layer caused by the wind interacting with the ground. The stochastic component is variable, and is a result of turbulence and interaction with the ground. Aerodynamic loads act primarily in the flapwise direction, as shown in Figure 1.7 [15].
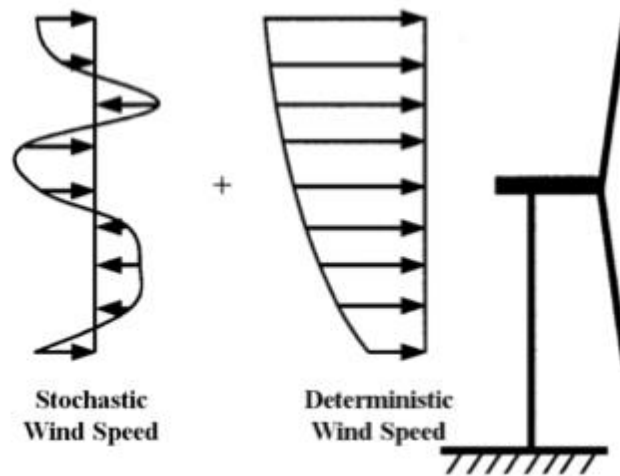
Figure 1.7: Stochastic and Deterministic Components of Wind [15]

1.4.2   Inertial Loads

Inertial loads consist of gravity and blade dynamic loads. Gravity loads are cyclic and interact with the blade in the lead-lag direction, shown in Figure 1.8. For larger blades, inertial loads reach the same level of magnitude as aerodynamic loads [15].

Figure 1.8: Gravity Load Affecting Wind Turbine Blade [15]

1.4.3   Load Phase Angle

Both aerodynamic and inertial loads are cyclic, and correspond to the azimuth angle. This implies that there is a relationship between the maximum flapwise load and the maximum lead-lag load. In 2004, White defined this relationship as the load phase angle [15]. The phase angle was defined as the angle between locations where the maximum flapwise and maximum lead-lag bending moments occur, as shown in Figure 1.9 [15].
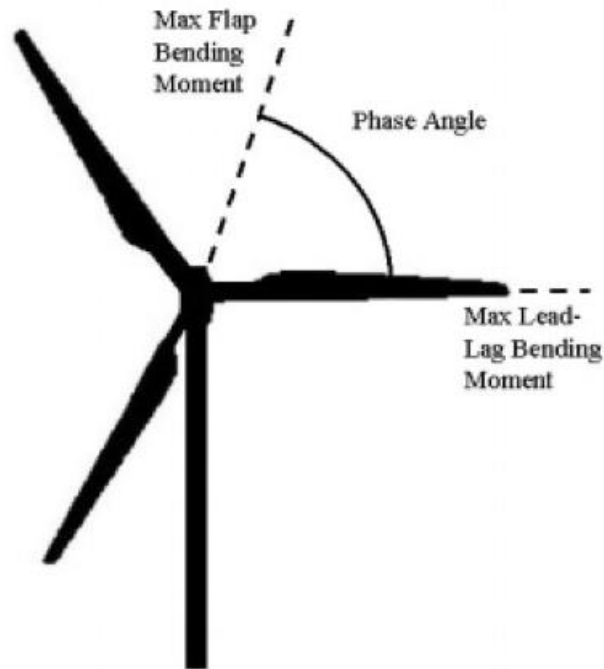
Figure 1.9: Phase Angle Definition [15]

White analyzed the loads of a simulated 1.5-MW pitch controlled, variable speed wind turbine subjected to IEC class Ia wind conditions. A statistical analysis of the phase angle for wind speeds up to 25 meters per second was performed [15]. The distribution of the phase angle for one such wind speed is shown in Figure 1.10.
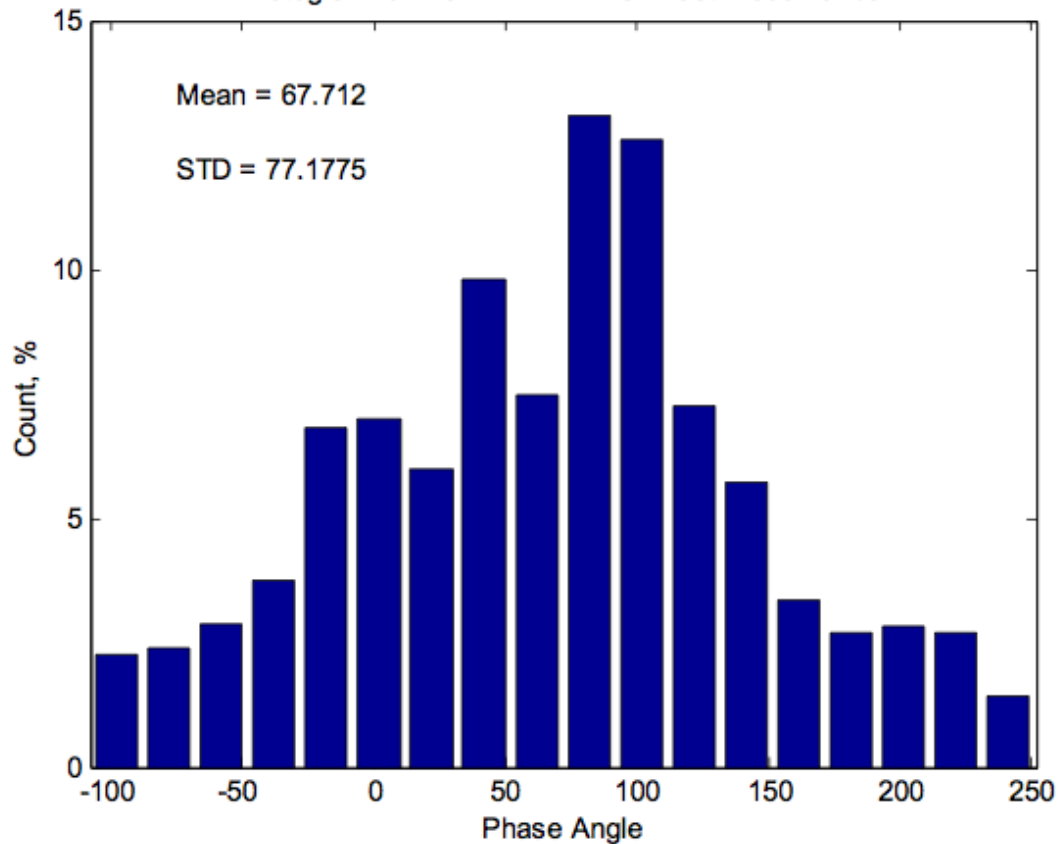
Figure 1.10: Distribution of Phase Angle in 9 m/s Wind Speed for Simulated 1.5 MW Wind Turbine [15]

It can be seen that the distribution is approximately Gaussian. This distribution was found for all wind speeds. The mean and standard deviation phase angle varies with wind speed [15].

An aggregate probability density function that approximates the above distribution was determined, and is shown in Figure 1.11. This shows that the mean phase angle for all wind speeds on the simulated 1.5-MW wind turbine blade is 72-degrees [15].
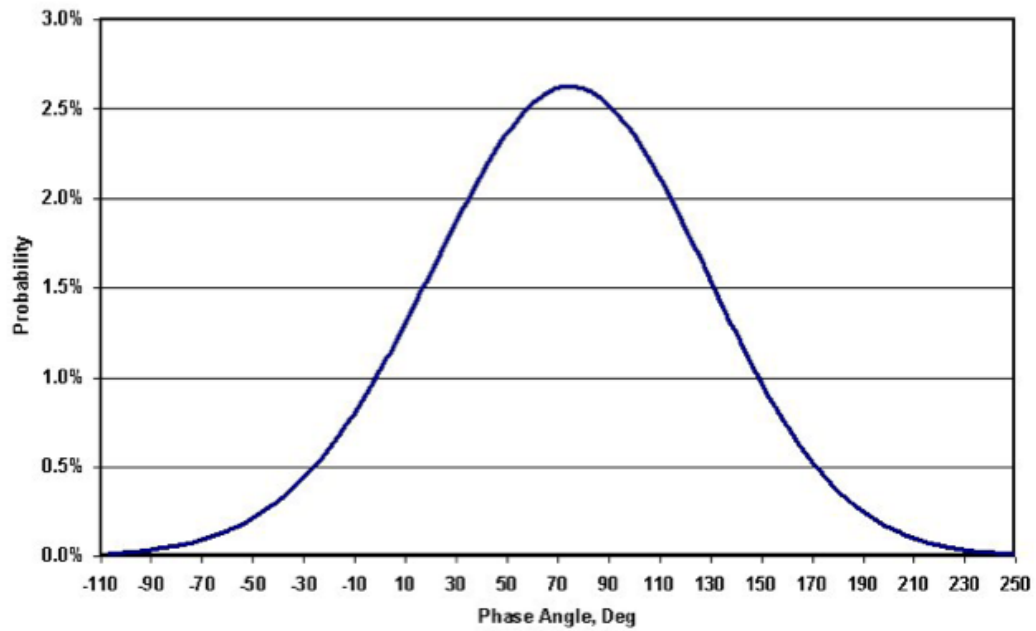
Figure 1.11: Aggregate Distribution of Phase Angle of All Wind Speeds Evaluated for a Simulated 1.5-MW Wind Turbine [15]

CHAPTER 2: FATIGUE TESTING OF WIND TURBINE BLADES

The design of wind turbine blades is rigorously tested in simulation, but variables such as manufacturing defects and material defects are not currently considered in simulation. Even when excluding defects, wind turbine blade dynamics are complex, yielding models that produce only approximate solutions. Full-scale blade testing can be used to validate assumptions made in the modeling process as well as identify material and manufacturing defects [15, 16, 25]. The IEC describes the purpose of a full-scale blade test as a demonstration of the reliability of the blade when tested to a specific limit state [16]. There are several variations of full-scale blade testing; however only design load-envelop testing is discussed in this thesis. Design load-envelop testing consists of static testing and fatigue testing that is not intended to fail the blade, rather it tests that the blade meets its structural design requirement. Static testing and fatigue testing methods are described below.

2.1   Full-Scale Blade Testing

2.1.1   Static Testing

Static testing is used to verify the ultimate strength of the blade. Static tests use winches, weights, or actuators to simulate the most extreme load cases the blade will be subjected to [15, 16]. The blade may be loaded in varying orientations through successive tests to simulate extreme load cases around the profile of the blade [16].

2.1.2   Fatigue Testing

Fatigue testing is used to validate the life performance of the blade. Fatigue tests use forced or resonant excitation of the blade at increased loads and load frequencies to simulate the lifespan of the blade. Increased loads and load frequencies are required to achieve the lifespan damage accumulation within a reasonable test duration [15]. In order to accurately fatigue the blade, the loads applied consider not only test duration, but also the fatigue properties of defects and load orientation [15].

Currently there are a few ways to fatigue test large wind turbine blades. Most methods have been adapted from fatigue testing smaller wind turbine blades. While these methods were adequate for testing the smaller wind turbine blades, they do not scale well for testing large wind turbine blades. A new fatigue test method has been developed to combine the strengths of current fatigue test methods while also being applicable for large blades. The following sections review current fatigue test methods and introduce the PhLEX methodology.

2.1.3   The Effect of the Load Phase Angle of Fatigue Testing

The importance of applying a controlled load phase angle was not well understood before the study done by White. Before this study, the only investigation into the load phase angle was done by Larwood *et. al.* In this study, the loads applied to a blade at a constant phase angle of 0-degrees and a constant phase angle of 90-degrees were compared. It was found that the test with a 0-degree phase angle imparted greater peak loads to the blade due to the maximum flapwise and

27

maximum lead-lag loads being in phase. This caused the blade to fail at an order of magnitude sooner than the test with a 90-degree phase angle [15, 24].

In the same study in which the phase angle was defined, White compared the effects on the accumulated damage of three fatigue tests with different phase angle distributions. The damage accumulation was determined for a simulated 1.5-MW wind turbine. The three phase angle distributions were a uniform distribution, a Gaussian distribution from section 1.4.3, and a constant phase angle of 72-degrees. The distributions were input into a finite element model (FEM) of the 1.5-MW blade strain data. The accumulate damage was then found using Miner's Rule. The accumulate damage at different nodes around the airfoil at a representative blade station for the different distributions are shown in Figure 2.1. As can be seen, there is little difference between the distributions at the first peak, but significant variation at the second peak. The uniform distribution yields the largest damage accumulation and the constant phase angle yields the lowest damage accumulation [15].
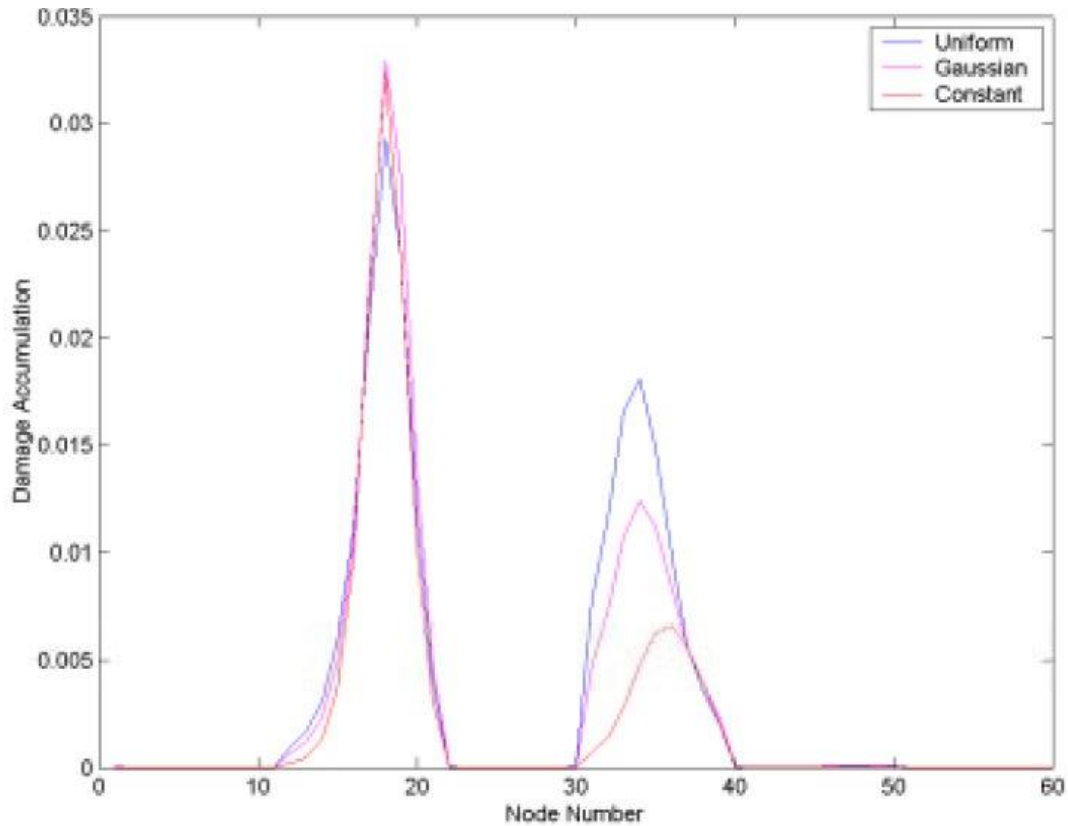
Figure 2.1: Total Damage Accumulation resulting from Varying Phase Angle Distributions [15]

The purpose of fatigue tests is to verify life performance, for this reason it is important to load test articles in a way that accurately represents loads seen during operation. If fatigue tests apply to much damage, the blades will begin to be over-designed, adding cost. If too little damage is applied, the blades may be subject to fail prior to scheduled end of life. This can increase costs and the risk of damage.

2.2   Current Dual-Axis Fatigue Test Methods

2.2.1   Forced Displacement

Dual-axis forced displacement uses hydraulic actuators to excite the blade below the flapwise fundamental frequency. This method allows control over the loads applied in each direction and the phase angle; however it has disadvantages. The low test frequency corresponds to long test durations, and test frequencies decrease with larger blades. The actuators used must be able to meet deflection requirements. Typical flapwise deflections at the tip of the blade are 20-percent of the blade length. The large stroke needed to test growing blade sizes requires specialty equipment, increasing test costs [15, 26, 27].
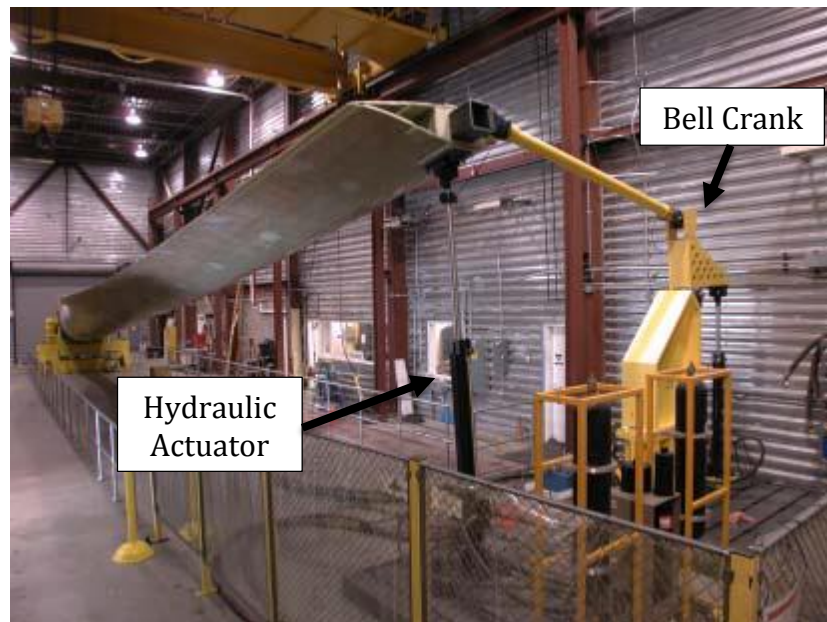
Figure 2.2: Dual-Axis Forced Displacement Test Set-Up

2.2.2 Resonant Testing

For smaller wind turbine blades that experienced predominately flapwise loading, a single-axis fatigue test was used. The single-axis tests used both forced actuation and resonant loading. Resonant is the favored load introduction method due to lower equipment and power costs. The single-axis resonant loading was developed by RISO. This method employs an electric motor to spin an eccentric mass. Masses are added to the blade in order to adjust the bending moment along the blade. The RISO resonance test method uses the speed of rotation to control the magnitude of the force applied. This causes a variable frequency throughout the test [15, 26].

A commercially available hardware set-up using resonant loading has been developed by NREL and MTS. The IREX hardware is a linear hydraulic actuator that mounts on a saddle attached to the blade. The IREX excites an inertial mass to load the blade. This method uses the stroke of the actuator, rather than the frequency, to adjust the magnitude of the load imparted to the blade [27, 28].
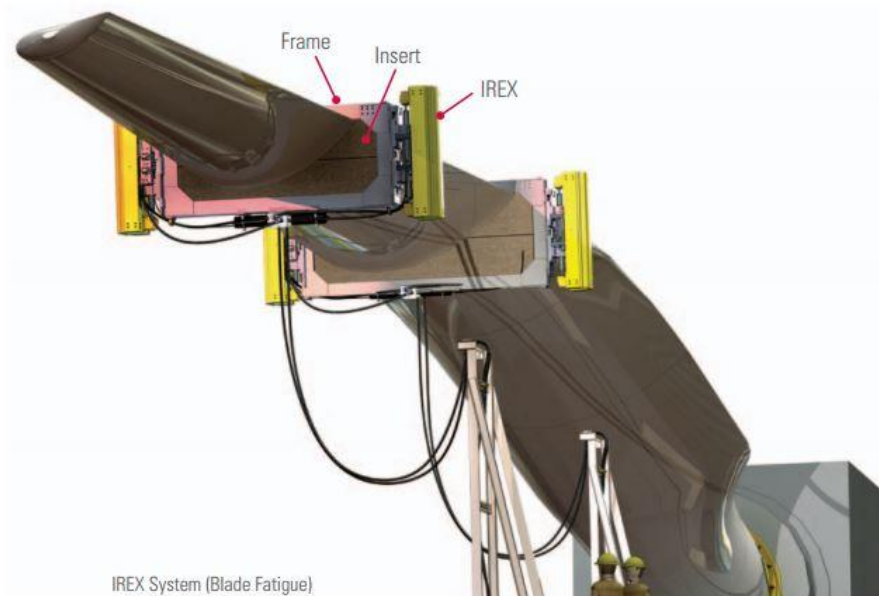
Figure 2.3: Dual-Axis Resonance Test Set-Up

For large turbine blades that require lead-lag fatigue testing, two, single-axis resonant tests are performed. Loading the blade in this way is not representative of loading seen in the field. The interaction of the flapwise and lead-lag moments is critical in properly fatiguing the blade. This method also has a long test duration, requiring two, separate tests [15, 27].

2.2.3   Resonant and Forced Displacement Testing

A combination of resonance and forced displacement testing was introduced called the blade resonance excitation (B-REX). The B-REX system uses a linear resonant actuator mounted on the blade to excite the flapwise fundamental frequency while a bell-crank mechanism, forced by a hydraulic actuator mounted to the floor, excites the lead-lag direction. This method operates at the flapwise fundamental frequency.

32

This gives a lower test duration than dual-axis forced displacement and single-axis resonant tests. This method also imparts a fixed 90-degree phase angle. While this is not the optimal testing condition, it is a significant improvement to single-axis testing [26]. This test method has lost favor to dual-axis resonant testing due to longer test durations as flapwise frequencies decrease and the increasing size and power of the bell-crank mechanisms needed to adequately load the blade. There are efforts being made to scale the B-REX system to modern blade sizes [29].

Figure 2.4: B-REX Test Set-up

2.2.4   Quantum Resonant Testing

The biaxial resonant fatigue testing excites the blade in the flapwise and lead-lag directions at their respective fundamental frequencies simultaneously. This method, developed by NREL, uses IREX hardware to excite the blade. Biaxial resonant testing

more accurately tests a blade than performing two, single-axis resonant tests, and can be completed in the time it takes to run the flapwise single-axis test [27]. The biaxial resonant test yields a uniformly distributed phase angle [15, 27]. The desired distribution of the phase angle is Gaussian with a 72-degree mean, as discussed in section 1.4.3.

Figure 2.5: Quantum Resonance Test Set-Up

A similar test method is being developed by the National Renewable Energy Center (NAREC) in the UK. This method excites both the flapwise and lead-lag directions simultaneously at their respective fundamental frequencies, with the blade pitched and masses added to the blade to optimize the load distribution. This method has the same advantages over single-axis testing as the quantum resonant test, but it also fails to consider the phase angle [30–32].

A second dual-axis resonant test method has been developed in a collaboration between NREL and the University of Colorado called base excitation test system (BETS). This system utilizes a spring element between the blade and test stand. Hydraulic actuators are mounted in parallel to the spring element, between the blade and test stand. The actuators excite both the flap and lead-lag direction simultaneously at the lead-lag natural frequency. In order to control the phase angle, an additional spring element is added to the dog bone assembly to force the flapwise fundamental frequency to the lead-lag frequency. This method has a lower test duration than other dual-axis tests, due to being run at the lead-lag fundamental frequency. It also requires smaller actuators because the actuators are located at the root where the smallest deflections occur. Having smaller actuators corresponds to having lower equipment costs and lower power requirements [33].
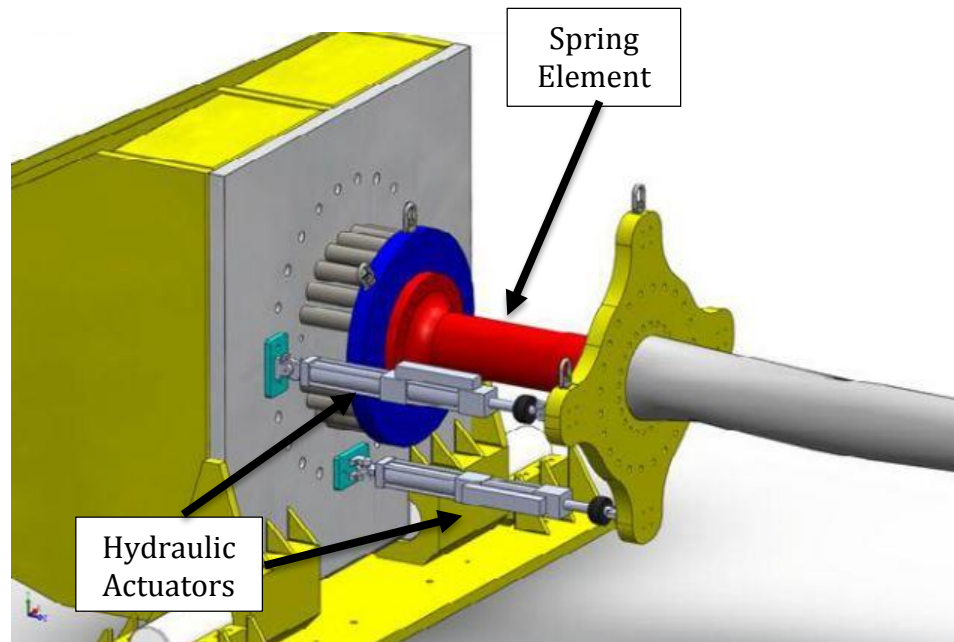
Figure 2.6: BETS Test Set-Up [44]

2.3   PhLEX Test Method

The dual-axis resonant PhLEX was developed in response to the shortcomings of current fatigue test methods. The PhLEX method utilizes a combination of resonant and forced displacement loading in order to lower power requirements while maintaining test accuracy. Three linear, resonant loading actuators excite the blade at the lead-lag fundamental frequency. Operating at the lead-lag fundamental frequency decreases test durations; the lead-lag direction is stiffer than the flapwise direction, creating a higher natural frequency. A fourth hydraulic actuator is mounted outboard of the resonant actuators. This actuator, called the PhLEX actuator, forces the flapwise direction to adhere to a first mode shape while applying the desired loading condition. The PhLEX actuator also allows control of the phase angle by controlling the flapwise displacement [34, 35].

The PhLEX system was developed in a collaboration between NREL and ERAU. The development of the PhLEX test method has gone through three distinct phases. The phases represents new evolutions of the test method brought on by the unique challenges of performing a phase-locked resonance test. In the following sections, the development of each phase and the challenge that initiated the next phase is briefly described.

2.4   PhLEX Development

2.4.1   Phase I

Phase I developed a quasi-static lumped mass-spring finite element model (FEM) of a wind turbine blade using Bernoulli beam theory. A 9-meter blade was used as a test specimen. The phase angle was controlled by adding an outboard actuator, known as the PhLEX actuator. The actuator was modeled as a spring and the corresponding stiffness was added to the appropriate nodes in the FEM. The required stiffness of the actuator in order to match the flap and edge fundamental frequencies was determined by using a non-linear optimization script in MATLAB [36]. An adaptive control algorithm was developed in Simulink to change the stiffness, or force, of the PhLEX actuator as needed. A peak detection algorithm was created to calculate the phase angle during the simulation. A PID controller was then used to adjust the PhLEX actuator force [37].

2.4.2   Phase II

Phase II of the PhLEX system development was to scale the model developed in Phase I to a 45-meter blade. Upon doing this, it was found that the stiffness required to modify the flap fundamental frequency to match the edge fundamental frequency created a fixed boundary condition at the PhLEX actuator attachment location. Phase I oversimplified the dynamics of the blade; therefore a linearized dynamic FEM was developed. The PhLEX actuator was no longer modeled as a spring, but as an input force at the lead-lag fundamental frequency. In order to minimize the

37

coupling of the flap and lead-lag deflections, the PhLEX actuator was tilted. The angle at which the PhLEX actuator attached to the blade was found using a custom conjugate gradient optimization routine written in MATLAB. The algorithm was used to determine the PhLEX actuator angle resulting in the minimum edge motion sensitivity to actuator force. The initial blade response was affected by the flap fundamental frequency, producing a noisy signal. To minimize the effects of the flap fundamental frequency, a feedback filter was developed to control the PhLEX actuator load signal [38].

2.4.3   Phase III

Phase II showed through simulation that the model developed could be controlled; however, the actuator power requirements were high [38]. Phase III developed a parallel control algorithm to more accurately control the blade while reducing energy requirements of the system [39].

The finite element model developed uses a lumped mass-spring-damper method. Each element was assumed to have six degrees of freedom, three in the axial directions and three torsional around each axis. The Bernoulli beam theory was used to develop the mass and stiffness matrices using blade designer-provided data. The damping matrix was developed using the stiffness matrix.

The two controllers used in this phase of the PhLEX system are a Model Reference Adaptive Controller (MRAC) and a proportional controller that uses the hyperbolic tangent function for saturation. The MRAC controls the lead-lag and flap deflection

by forcing the blade to a specified set of deflections determined from the manufacturer provided bending moments. Since there was no information provided by the manufacturer concerning the edge bending moments for the 9-meter blade; the edge moments were derived from the edge bending moments of the larger 45-m blade. The pole-placement filter from Phase II was also implemented to ensure a clean input signal. The proportional controller controls the phase angle. The hyperbolic tangent function is used as a saturation limit for the phase angle between 60-80 degrees. The phase angle is calculated using a peak detection algorithm for the lead-lag and flap displacements [39].

2.5 *PhLEX Model Predictions*

2.5.1   Power Requirements of PhLEX actuator

The power requirement of the PhLEX actuator was predicted for varying blade lengths. The velocity and force required to achieve the target root bending moment were determined from the model with the following assumptions. The actuators were assumed to be at the 18-percent and 75-percent blade stations. The combined weight of the two saddles on the blade was assumed to be half the weight of the blade, with 20-percent of the weight at the outboard saddle. A critical damping ration of 2-percent was assumed for each blade length. Table 2.1 summarizes the results [40].

Table 2.1: Predicted Power Requirements for PhLEX Actuator

Blade Length	Excitation Frequency (Hz)	Displacement (m)	Force (kN)	Power (hp)
9-meter	3.05	0.08	4.37	0.53
45-meter	0.66	0.33	74.76	8.28
70-meter	0.26	0.32	279.53	11.53
90-meter	0.21	0.45	672.16	32.18

2.5.2   Test Duration

The test duration of the PhLEX test method was predicted for a 9-meter blade. The test duration of the of the PhLEX test method was compared to a two, single-axis resonance test and a dual-axis quantum resonance test. It is assumed that all tests will fulfill the damage requirement at every cycle [40]. The results are shown in Figure 2.7.
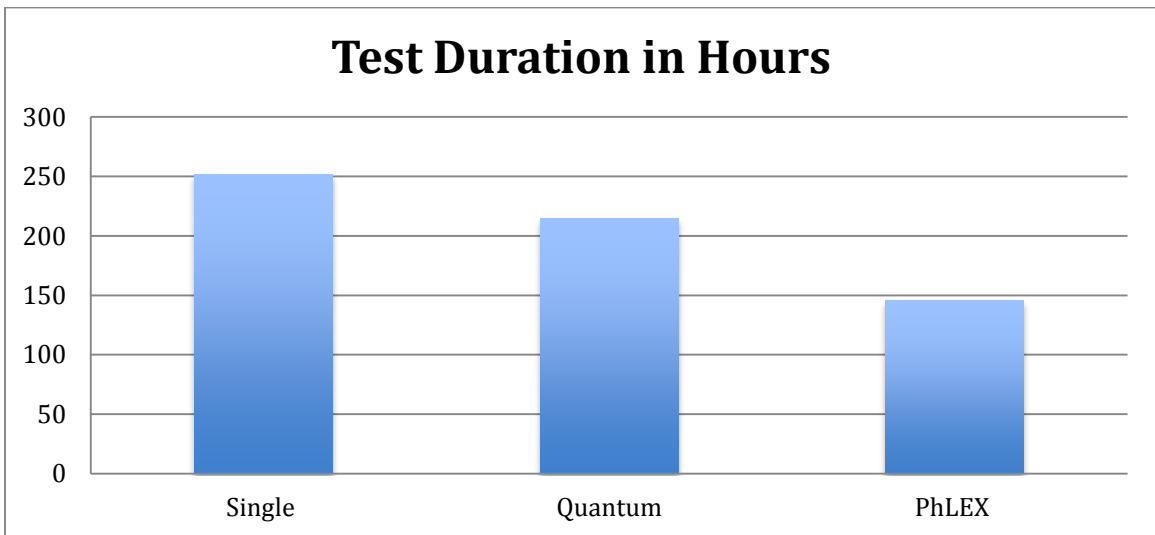
Figure 2.7: Test Duration of Fatigue Test Methods for a 9-meter Blade

2.6   Scope of Thesis

The primary goal of this thesis is to perform a proof-of-concept test for a dual-axis resonant phase-locked excitation (PhLEX) fatigue test method and evaluate the results. The proof-of-concept test was conducted at the NWTC, a part of NREL, in July 2012. The PhLEX proof-of-concept test set-up and the result and conclusions of the proof-of-concept test are presented in this thesis.

CHAPTER 3: PROOF-OF-CONCEPT TEST

3.1   Test Scope

The purpose of the proof-of-concept test was to demonstrate the PhLEX fatigue test method. There were two primary objectives during this test:

1. Show robustness of PhLEX control strategy.

2. Show ability to control phase angle to 72-degrees by cycle-to-cycle load introduction.

The proof-of-concept test was conducted at the NREL's NWTC. Details of the test article and test set-up are given in the following sections. The Test Plan is reproduced in Appendix C.

3.2   Test Article

The test article selected was the 9-meter CX-100. The CX-100 blade was chosen due to the ease of integrating the PhLEX test hardware into hardware available for this blade. The CX-100 is a prototype blade designed by Sandia National Laboratory (SNL) and manufactured by TPI Composites. The CX-100 blade design is based on the ERS-100 blade with a full-length carbon fiber spar cap. The CX-100 was developed to evaluate the use of carbon fiber in subscale blades [41-43]. The planform of the CX-100 is shown in Figure 3.1.
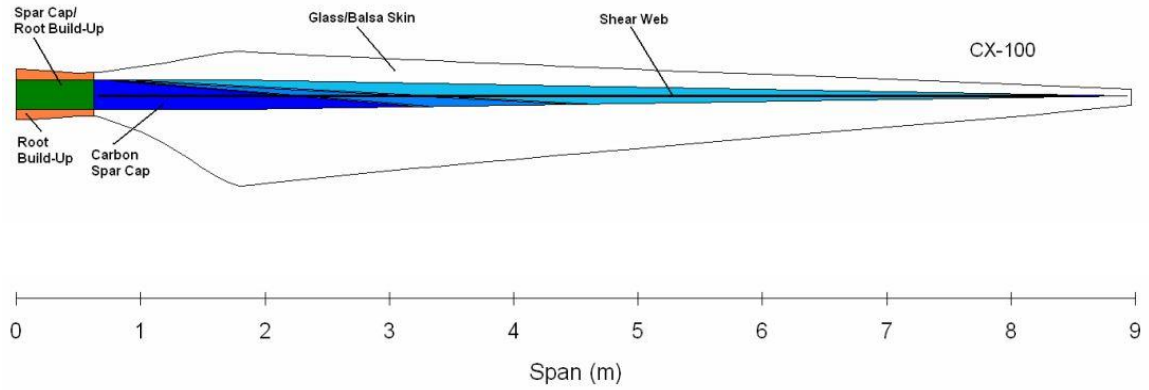
Figure 3.1: Top Planform of the CX-100 Blade [42]

The normalized blade properties of the CX-100 are shown in Table 3.1.

Table 3.1: Normalized Blade Properties of CX-100 Blade [43]

Normalized Blade Station	MPL	Chord	Flat EI	Edge EI	GJ	Twist
0.00	1.0000	0.3446	1.0000	1.0000	1.0000	1.0000
0.02	1.0000	0.3446	1.0000	1.0000	1.0000	1.0000
0.07	0.2618	0.3272	0.2200	0.3616	0.2343	0.8378
0.11	0.2663	0.5508	0.1939	0.5011	0.1839	0.7027
0.16	0.2478	0.8325	0.1367	0.5072	0.1603	0.5912
0.20	0.1510	1.0000	0.1229	0.3586	0.0970	0.4966
0.24	0.1390	0.9380	0.0967	0.3137	0.0836	0.4189
0.36	0.1188	0.8064	0.0563	0.1898	0.0474	0.2804
0.47	0.0976	0.6825	0.0287	0.1093	0.0258	0.1959
0.58	0.0787	0.5634	0.0135	0.0571	0.0120	0.1351
0.69	0.0594	0.4482	0.0044	0.0265	0.0050	0.0912
0.80	0.0431	0.3349	0.0013	0.0095	0.0018	0.0473
0.91	0.0251	0.2246	0.0002	0.0022	0.0004	0.0135
1.00	0.0175	0.1162	0.0000	0.0003	0.0001	0

Two saddles were added to the blade for load introduction. The location and mass of the saddles is given in Table 3.2.

Table 3.2: Mass Properties of Saddles on Test Article during Proof-of-Concept Test

Saddle	Saddle Distance from Root (m)	Saddle Weight (kN)
UREX saddle	1.6	5.712
PhLEX saddle	6.75	1.419

3.3   Test Set-Up

3.3.1   Facility Configuration

The proof-of-concept test took place at NREL's NWTC on a 1360 kN·m test stand.

The test stand was tilted 4.4-degrees in order to accommodate the PhLEX actuator.

A schematic of the blade mounting is shown in Figure 3.2.
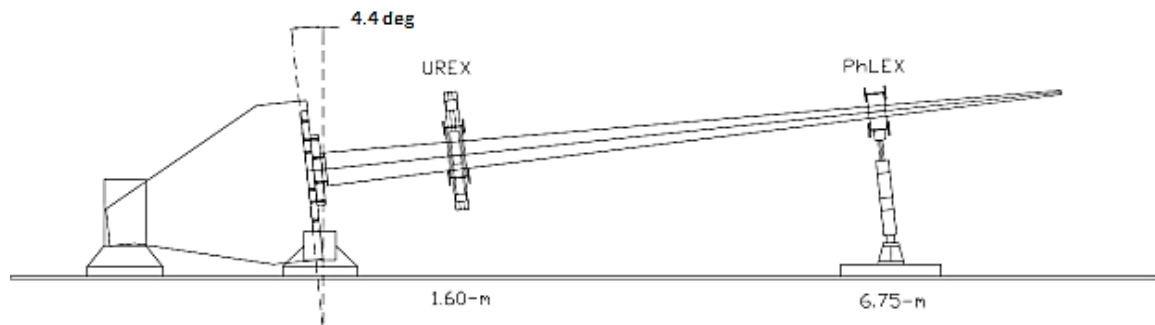
Figure 3.2: Test Stand Rotation

3.3.2   Blade Orientation

The blade was installed on the test stand so that the HP surface was upward and the

local chord at the 7-meter blade station, 7 meters out measuring from the root, was

0-degrees from the horizontal. The orientation of the blade was determined using an optimization script to minimize coupling between the lead-lag and flapwise directions [39].

3.3.3   Load Introduction

The loads were introduced to the blade by three actuators at the 1.60-meter blade station and one actuator at the 6.75-meter blade station. The actuators were coupled to the blade through saddles. The saddles were constructed of wood forms sandwiched by two I-beams. The wood form had the airfoil section of the test article removed. A ¼-inch rubber strip was between the blade and the wooden form. Saddles are used to transfer loads evenly to the blade. The rubber strips are used to fill gaps between the wood form and the blade and prevent slipping during the test.

Three UREX actuators were mounted on the saddle at the 1.60-meter station. Two of the UREX actuators were mounted in the flapwise direction, designated as UREX North and UREX South. A third UREX actuator was mounted in the lead-lag direction, designated UREX Edge. UREX actuators utilize a resonant loading method. The actuators are mounted only to the saddle, exciting a small mass at the desired resonant frequency. The motion of the mass then translates movement to the blade.

The fourth actuator was mounted at the 6.75-meter blade station. This actuator was designated the PhLEX actuator. The PhLEX actuator is a single-ended actuator that is mounted directly to floor. The PhLEX actuator is mounted with an angle of

8.3-degrees from the vertical in order to decouple the flap and lead-lag directions. The test set-up is shown in Figure 3.3.
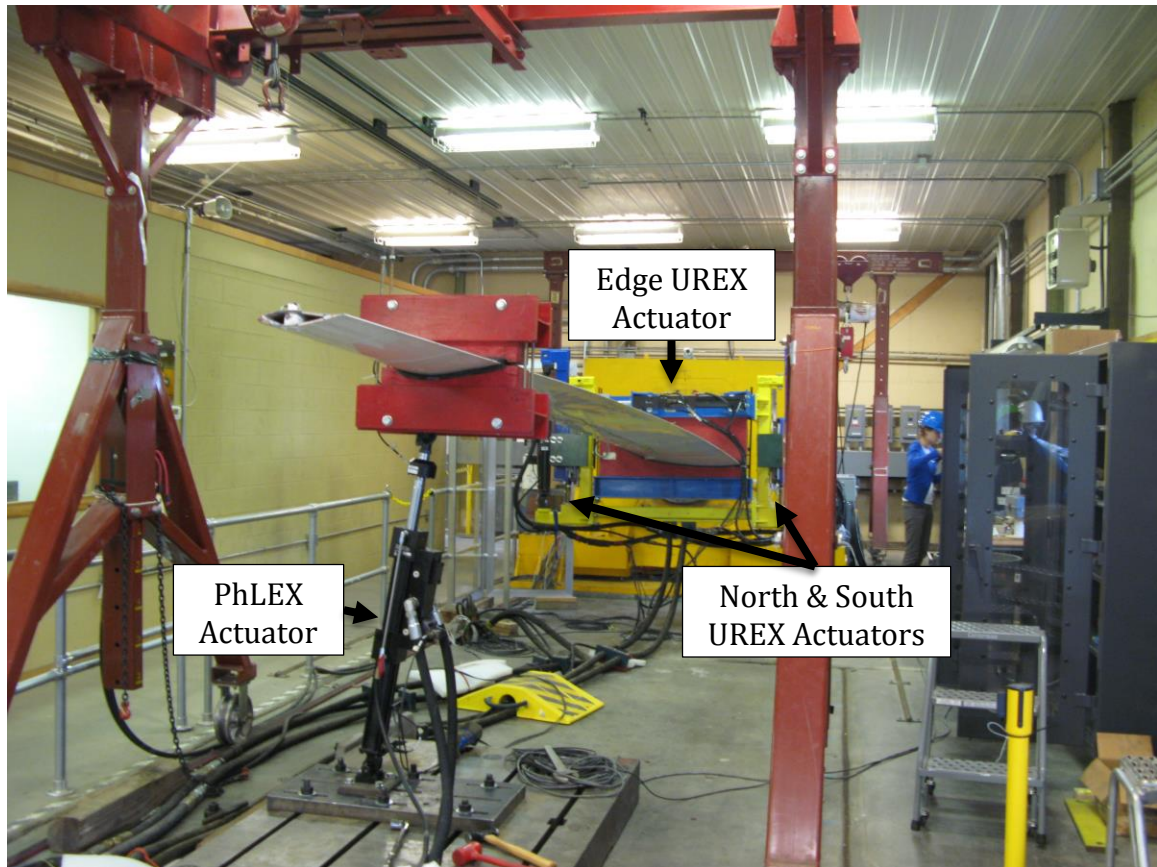
Figure 3.3: Proof-of-Concept Test Set-Up

The locations of the saddles were not optimized for this test. The locations of the saddles, and, therefore the locations of the load introduction, were selected due to the availability saddle equipment for the 1.6-meter and 6.75-meter blade stations.

3.3.4 Instrumentation of Blade

The test article was instrumented in order to evaluate the test and to provide feedback to the controller. The instrument of the blade is described below. The locations of the instrumentation of the blade is described in the Test Plan reproduced in Appendix A.

A load cell was placed between the PhLEX actuator and the 6.75-meter saddle to capture the load applied to the blade by the PhLEX actuator.

Each actuator had an LVDT to monitor the actuator displacement.

Four, biaxial DC accelerometers were in place along the spanwise direction of the blade on the HP surface spar cap. They were located at the 2250-mm, 4500-mm, 6650-mm, and 8000-mm blade stations.

A total of 23 strain gauges were installed on the blade on both the HP and LP surfaces. The airfoil at the 3.2-meter station had strain gauges around the local airfoil to monitor the effect the phase angle had on the strain distribution around the profile. The 3.2 –meter station was selected for the airfoil strain gauges because it was predicted to have the highest strains due to its proximity to maximum chord.

3.4   Control Strategy

MTS 793 software will be used to control the actuators. The UREX actuators will be controlled with frequency and displacement. The feedback signals for the UREX actuators will be the accelerometers and the LVDTs. The PhLEX actuator will be

controlled with force and displacement. The feedback signals for the PhLEX actuator

will be the load cell and the LVDT.

Chapter 4: TESTS PERFORMED DURING PROOF-OF-CONCEPT TEST

The proof-of-concept test was conducted to evaluate the PhLEX test method. In addition to the PhLEX test method, two, single-axis resonance tests, and a quantum resonance test were to be performed. The full test matrix is shown in Table 4.1.

Table 4.1: Proof-of-Concept Test Matrix

Test Description	Type	% of Target Root moment Range	Number of Cycles
PhLEX Only	Static	50%	1
PhLEX Only	Static	100%	1
Single-Axis Flap	Fatigue	100%	5k
Single-Axis Edge	Fatigue	100%	5k
Dual-Axis Quantum	Fatigue	50%	5k
Dual-Axis Quantum	Fatigue	75%	5k
Dual-Axis Quantum	Fatigue	100%	5k
Dual-Axis PhLEX	Fatigue	25%	5k
Dual-Axis PhLEX	Fatigue	50%	5k
Dual-Axis PhLEX	Fatigue	75%	5k
Dual-Axis PhLEX	Fatigue	100%	5k

Some of the tests described in the test matrix were unable to be performed due to complications with the test set-up and time restrictions. The tests that were performed are given in Table 4.2.

Table 4.2: Tests Performed during Proof-of-Concept Test

Test Description	Type	% of Target Root moment Range	Number of Cycles
Single-Axis Flap	Fatigue	100%	5k
Single-Axis Edge	Fatigue	100%	5k
Dual-Axis Quantum	Fatigue	5%	5k
Dual-Axis PhLEX	Fatigue	3%	5k

The following sections outline the complications encountered and the tests performed during the proof-of-concept test.

4.1   *Feedback Signal Disturbance*

A disturbance acting at approximately ten times the excitation frequency appeared on all signals relaying blade dynamics (i.e. accelerometers, strain gauges, and PhLEX load cell). The accelerometers and PhLEX load cell signals were used as feedback signals to control the actuators. The disturbance created a beat pattern with the excitation frequency, causing large peaks in the feedback control signals. The large peaks tripped the safety limits of the control system. In order to conduct the proof-of-concept test, without sacrificing safety, the applied moments were decreased for the five thousand cycles test demonstrations.

Several efforts were made to filter the disturbance from the feedback signals; however none were successful. The cause of the disturbance was unknown for the duration of the test. In an investigation after the test, the cause has been attributed to valve flutter in the PhLEX actuator. This conclusion is supported by the disturbance remaining at approximately ten times the excitation frequency throughout the test.

4.2   *Overview of Tests*

The control method of Phase III described in section 2.4.3 was unable to be tested due to the limitations of the control software available. Various other control

methods were tested and an effective control method was determined. The control

methods evaluated and results of these methods are presented in the following

sections. A full list of tests performed is given in Appendix B.

4.2.1   Control Diagram

A basic control diagram is presented in Figure 4.1. This control strategy was used

throughout all tests. The UREX actuators were in displacement control with LVDT

feedback for all tests. The command and feedback signals of the PhLEX actuator vary

for each test, and are described in the following sections.
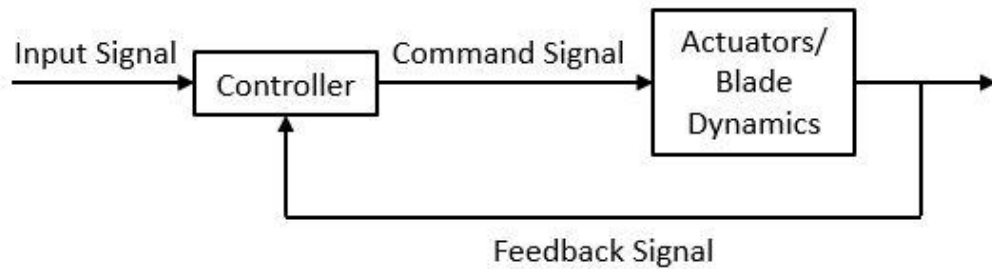
Figure 4.1: Generic Control Diagram Used in PhLEX Proof-of-Concept Test

4.2.2   Dual Compensation Control

The PhLEX test was run with the PhLEX actuator in dual compensation control with

the PhLEX LVDT signal as the primary feedback and the PhLEX load cell as the

secondary feedback. A control diagram of this method is shown in Figure 4.2.
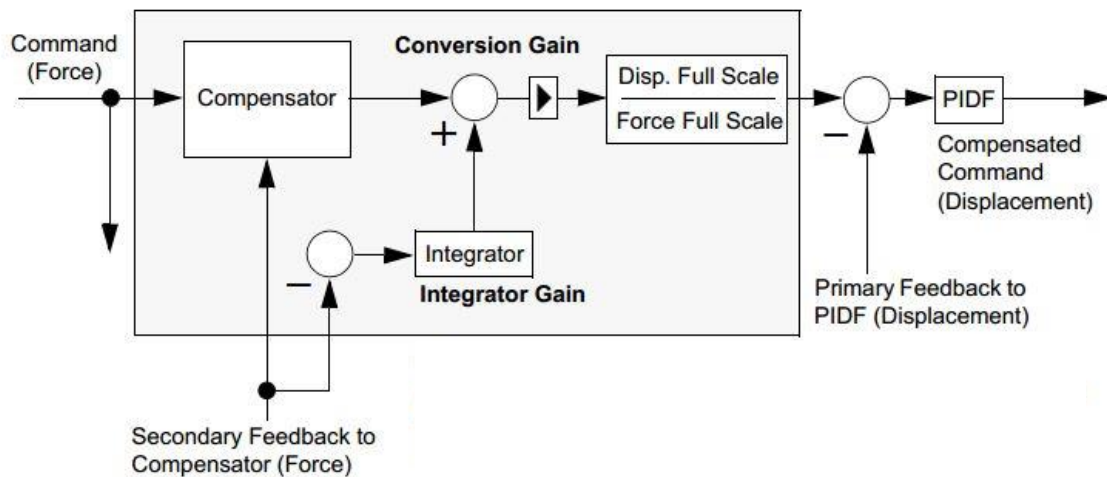
Figure 4.2: Dual Mode Control Diagram [51]

This control method was able to produce a stable deflection in both lead-lag and flapwise directions while marinating a constant phase angle. This control method was used for the PhLEX test results that are analyzed in Chapter 5 of this thesis.

4.2.3   Force Control and Displacement Control

The PhLEX test was run with the PhLEX actuator in force control with PhLEX load cell feedback. This method caused the system to be unstable.

The PhLEX test was run with the PhLEX actuator in displacement control with PhLEX LVDT feedback. This method was assumed to have not worked due to the presence of the disturbance on the blade dynamic signals. However, this method could be revisited if the disturbance signal could be eliminated.

CHAPTER 5: PROOF-OF-CONCEPT TEST DATA POST-PROCESSING RESULTS

Several variations of the PhLEX test method were conducted during the proof-of-concept test. Post-processing of the test data was only performed on one of these variations.

5.1   Signal Disturbance Filter

A three second snapshot of the flapwise accelerometer data is shown in Figure 5.1. The disturbance discussed in section 4.1 can clearly be seen on the signals.
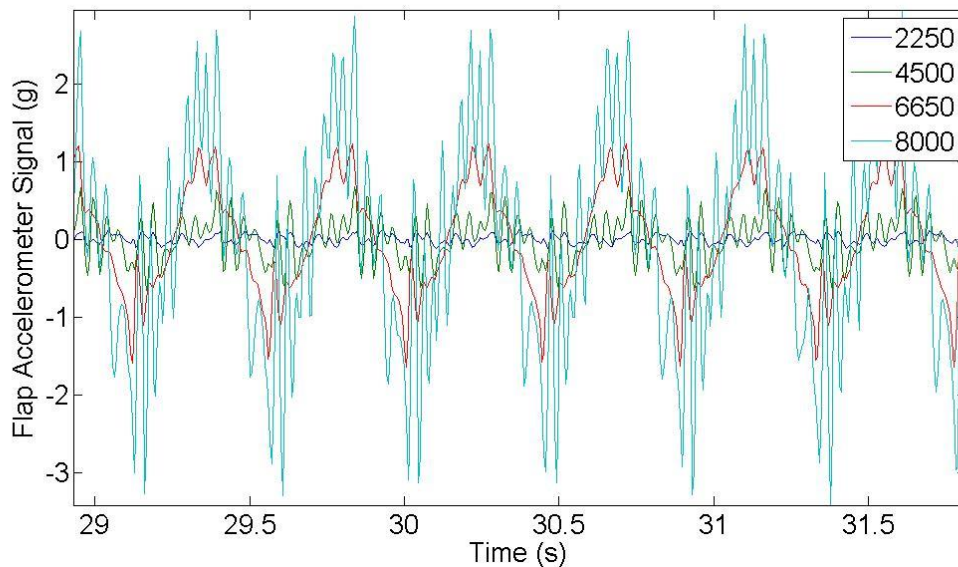
Figure 5.1: Flapwise Accelerometer Signals during PhLEX Test

A low pass filter with a 10-Hz cut-off frequency was used to filter the signals prior to evaluation. Figure 5.2 shows the un-filtered and filtered signal of the 6650-mm station accelerometer.

53

Unfiltered Accelerometer Signal

Time

Frequency (Hz)

Filtered Accelerometer Signal

Time
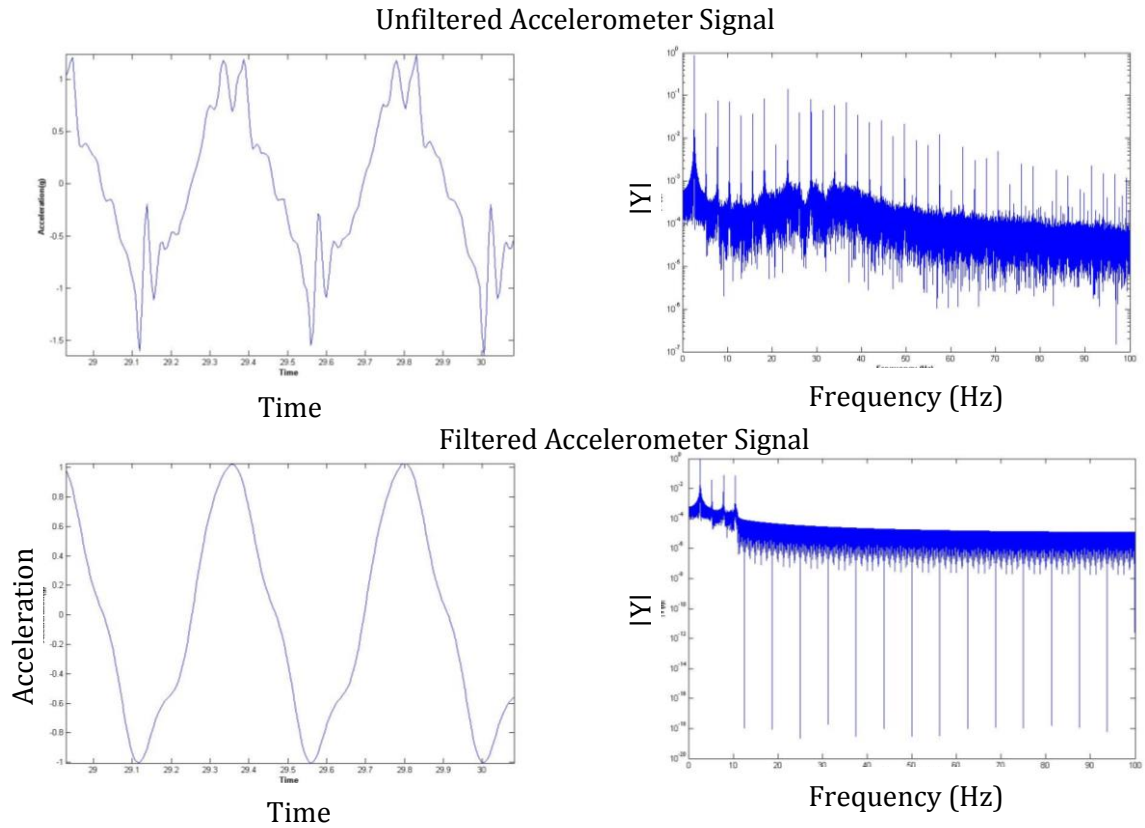
Frequency (Hz)

Figure 5.2: Filter and Un-Filtered Accelerometer Signals with Corresponding Frequency Amplitude Spectrum

5.2   Dual-Axis PhLEX Test

The test used to represent the PhLEX fatigue method utilized the PhLEX and the

Edge UREX actuators. The North UREX and South UREX actuators were unused, but

remained on the blade. Both actuators were run at 2.613-Hz with a 0-degree phase

lag. The PhLEX actuator was set to 1-degree from the vertical. The blade saw

clockwise, dual-axis motion. The LVDT signals for the PhLEX test are shown in

Figure 5.3.

54
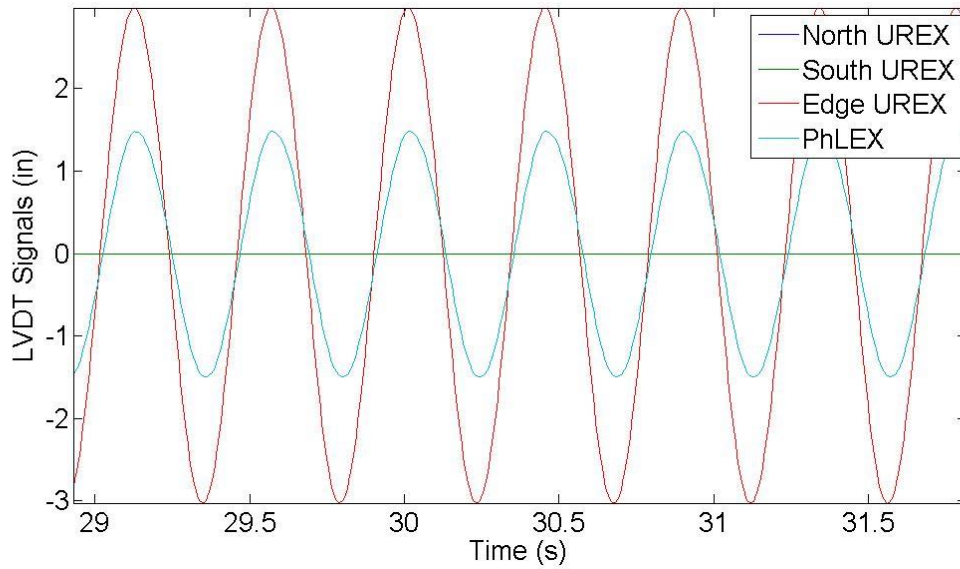
Figure 5.3: LVDT Signals during the PhLEX Test

5.2.1 PhLEX Applied Moments

A MATLAB script was created to evaluate the data. The accelerometer data was mean centered. A peak and valley detection algorithm was developed to identify the peak accelerations for each accelerometer signal. A snapshot of the blade acceleration in time was then created for each peak detected on all accelerometers. The lead-lag and flapwise accelerations were evaluated separately. The snapshots of the blade for each accelerometer were then compared. The shape of the blade during the snapshot was similar for all accelerometer locations. The 6650-mm station accelerometer was chosen for subsequent operations.

A sixth degree polynomial was fit to the blade accelerations using the MATLAB function *lsqcurvefit*. Figure 5.4 and Figure 5.5 shows the peak accelerations and the curve fit polynomials for the lead-lag and flapwise directions.
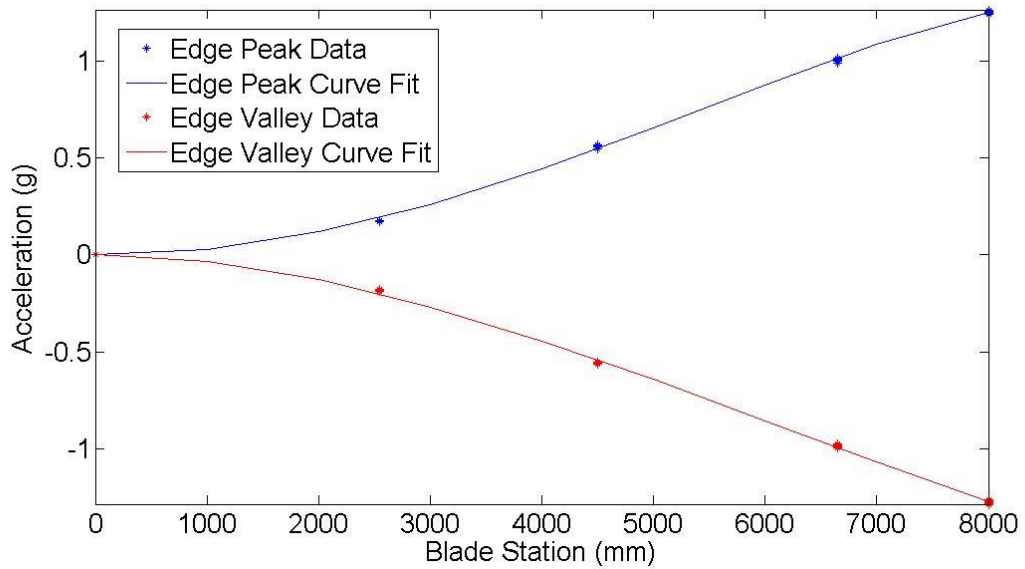
Figure 5.4: Lead-Lag Peak and Valley Accelerometer Data during PhLEX Test
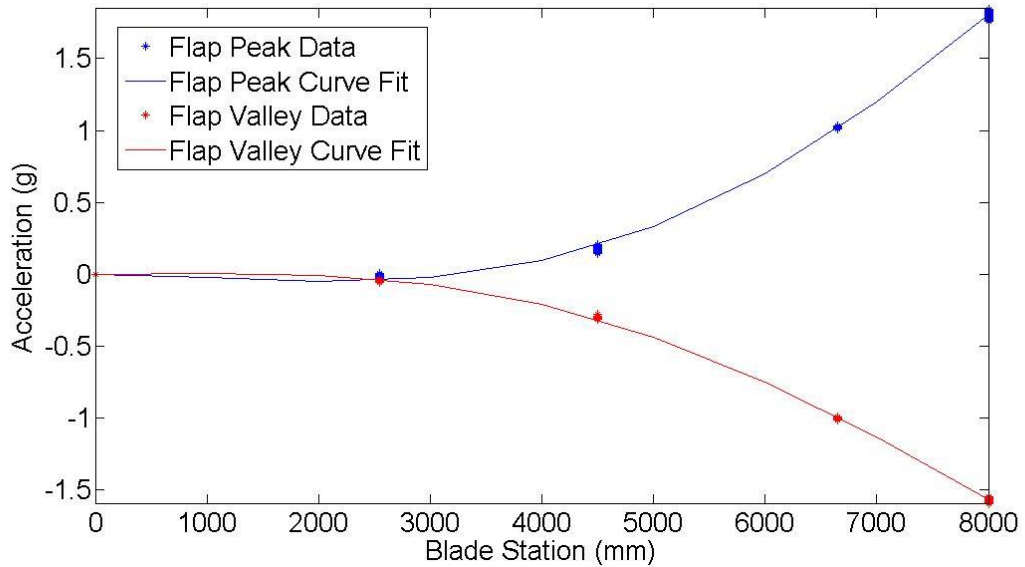
Figure 5.5: Flapwise Peak and Valley Accelerometer Data during PhLEX Test

56

The moments applied to the blade during testing were determined using the forces

applied to the blade during the test. The forces at each meter along the blade were

determined using Equation 5.1.

$$F = m\ddot{x}$$

Where:
F = force applied to blade
m = mass
$\ddot{x}$ = acceleration

The acceleration used was determined from the polynomial fit to the peak

acceleration data. The mass at each station was interpolated from mass per length

data given in Table 3.1.

The moments applied during the test were compared to the target moments given

by the blade designed for the flapwise direction. Target loads for the lead-lag

direction were not provided. The PhLEX test only loaded the blade to 3-percent of

the target root bending moment. In order to more accurately compare the bending

moment distribution, the target bending moment and applied bending moments

were normalized. The normalized flapwise and lead-lag moments applied to the

blade are shown in Figure 5.6 and Figure 5.7.

57
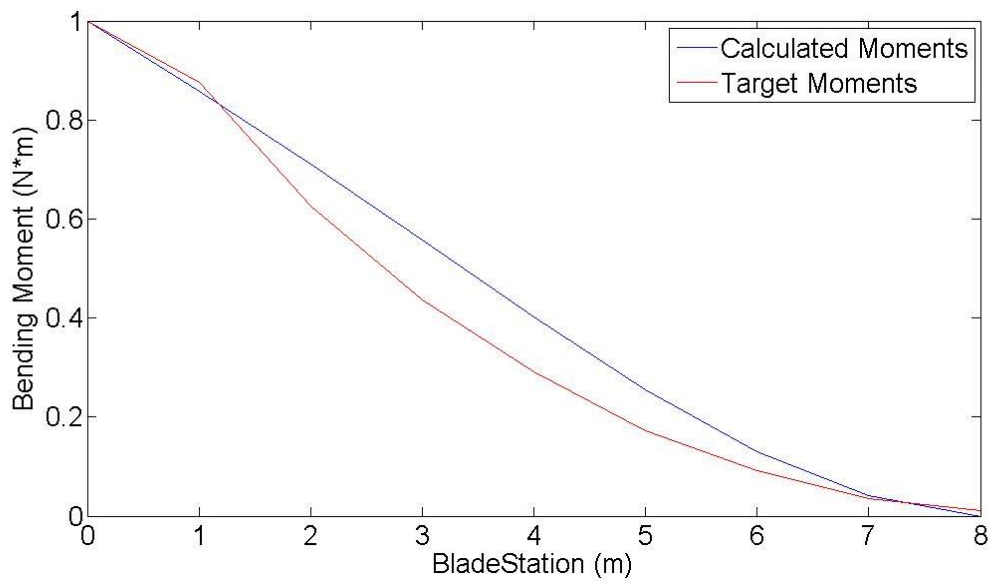
Figure 5.6: Target and Calculated Flapwise Bending Moments during PhLEX Test
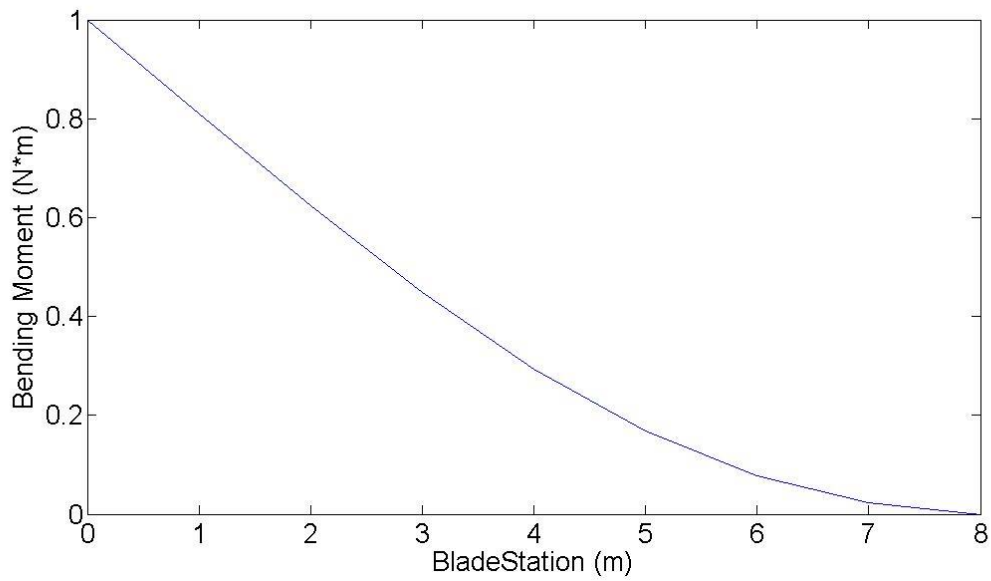
Figure 5.7: Calculated Lead-Lag Bending Moments during PhLEX Test

5.2.2   PhLEX Phase Angle

The unfiltered accelerometer data was integrated to deflection data using an algorithm developed for this thesis. The algorithm used the trapezoidal rule to integrate between data points [45, 46]. There was significant drift in the integration. The drift was assumed to be caused by gravity acting on the accelerometers at all times [47]. In order to remove the drift, a high-pass filter with a 1-Hz cut-off frequency was used to deter error propagation during integration to the deflection data [47].

The same peak/valley detection and curve fit analysis developed for the acceleration data was used on the deflection data. The peak deflections and the curve fit polynomial of the deflection data are shown in Figure 5.8 and Figure 5.9.
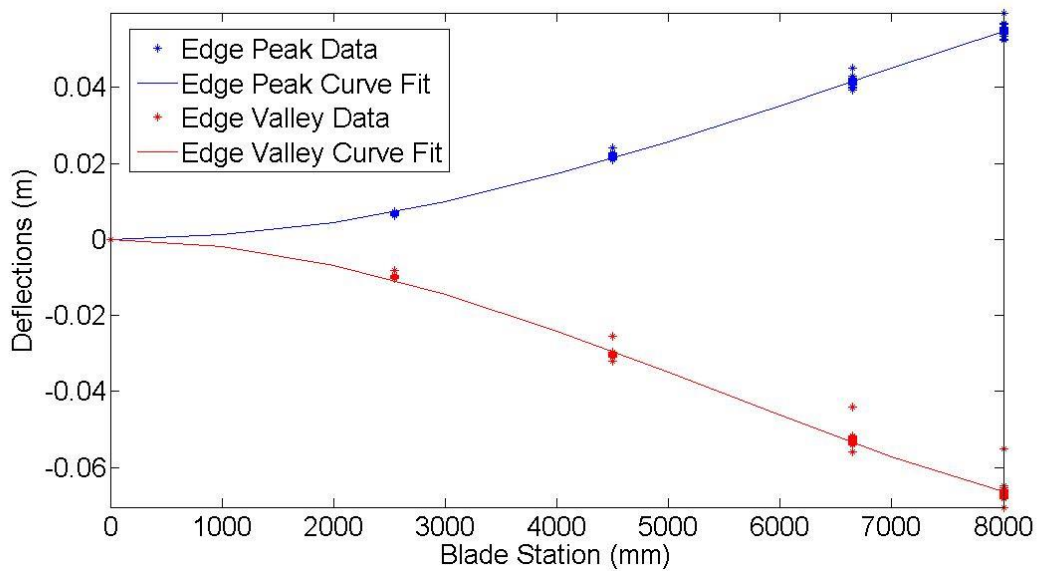
Figure 5.8: Lead-Lag Peak and Valley Deflection Data during PhLEX Test
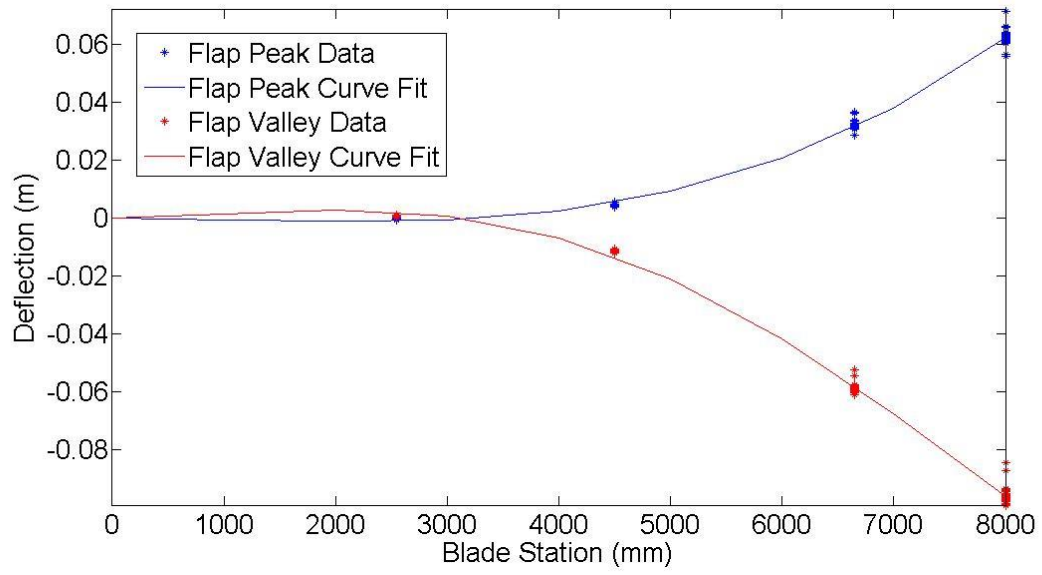
Figure 5.9: Flapwise Peak and Valley Deflection Data during PhLEX Test

The phase angle was determined from the time difference between the peaks of the lead-lag and flapwise deflection signals. A Lissajous figure is a visual representation of the phase shift between two signals [48, 49]. The phase shift can be determined from the eccentricity of the oval, as shown in Figure 5.10.

$$B/A = \sin(\phi)$$
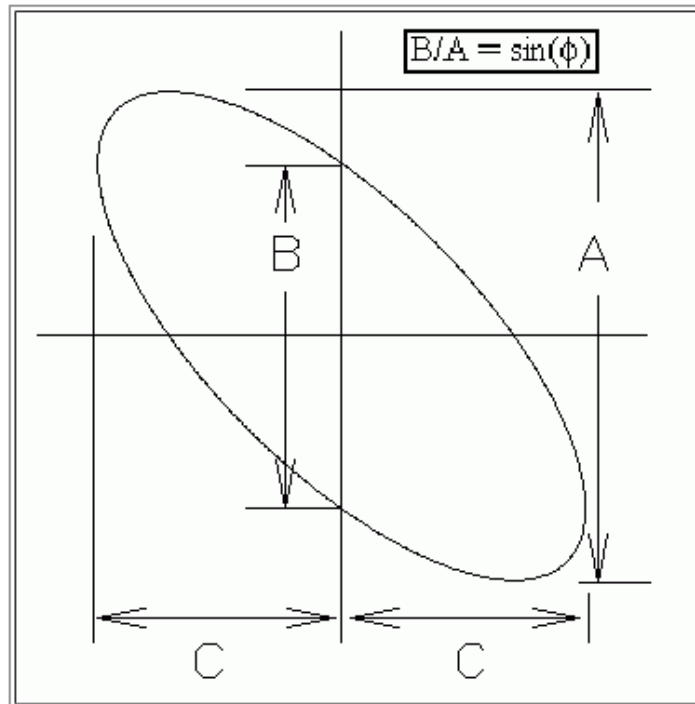
Figure 5.10: Phase Angle Determination from a Lissajous Figure [39]

The Lissajous figures of the deflection data at each accelerometer location is shown in Figure 5.11. The largest oval is the deflection at the 8000-mm blade station.
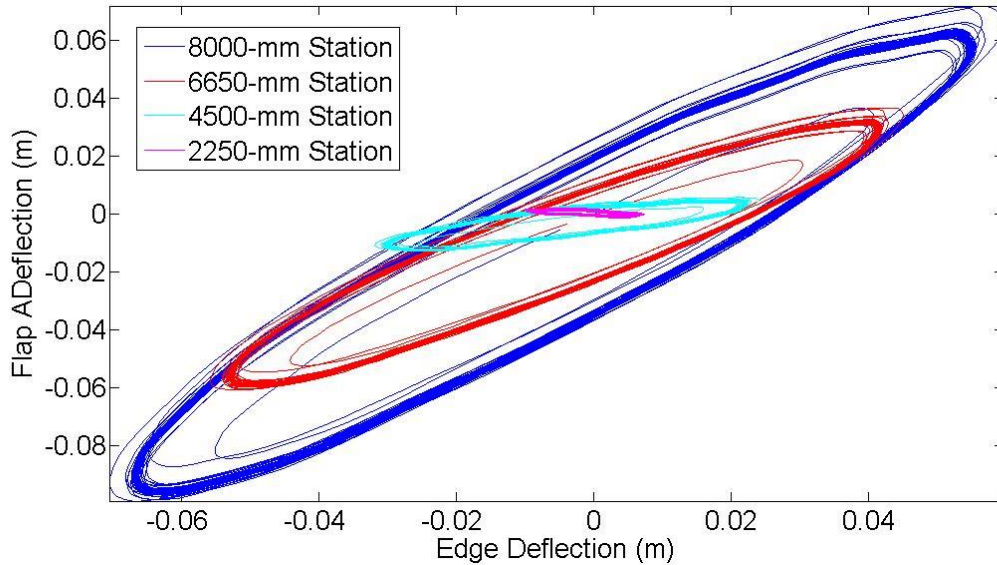
Figure 5.11: Lissajous Figure of Lead-Lag and Flapwise Deflection Data during PhLEX Test

5.3   Quantum Resonance Test

The test used to represent the Quantum Resonance test method utilized the North, South, and the Edge UREX actuators. The North UREX and South UREX actuators were run at 2.6-Hz and had an alternating deflection of 0.5 inches. The relative movement between the North and South UREX actuators was fixed. The Edge UREX actuator was run at 1.9-Hz and had an alternating deflection of 1 inch. There was an 180-degree phase lag between the Edge UREX actuator and North and South UREX actuators. Figure 5.12 shows the LVDT signals of the UREX actuators.
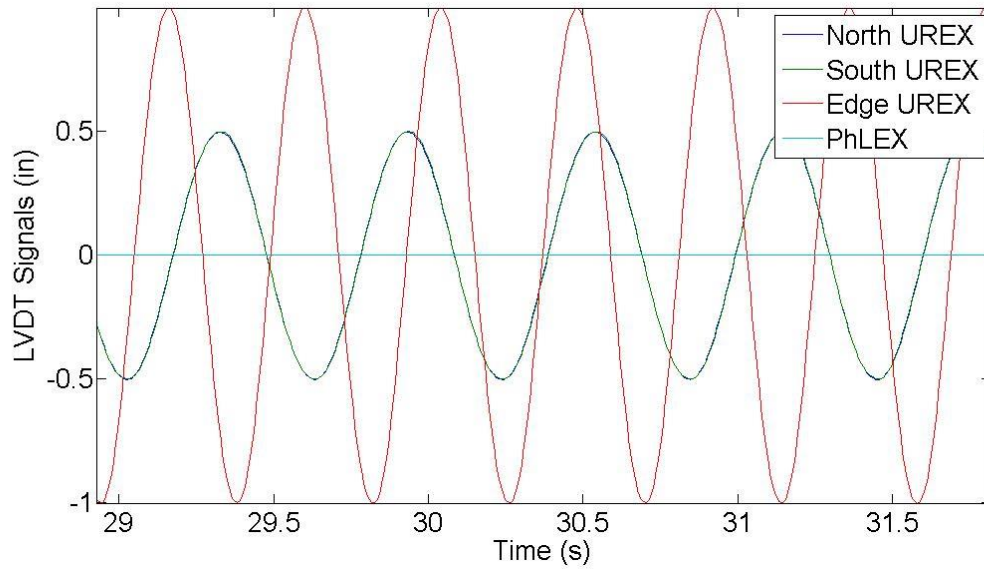
Figure 5.12: LVDT Signals during Quantum, Resonance Test

5.3.1 Quantum Resonance Applied Moments

The same analysis used on the PhLEX test data was used on the Quantum resonance

data. The accelerometer data was filter and put through a peak and valley detection

algorithm. The peak and valley detection of the accelerometer data and the curve fit

polynomial are shown in Figure 5.13 and Figure 5.14.

63
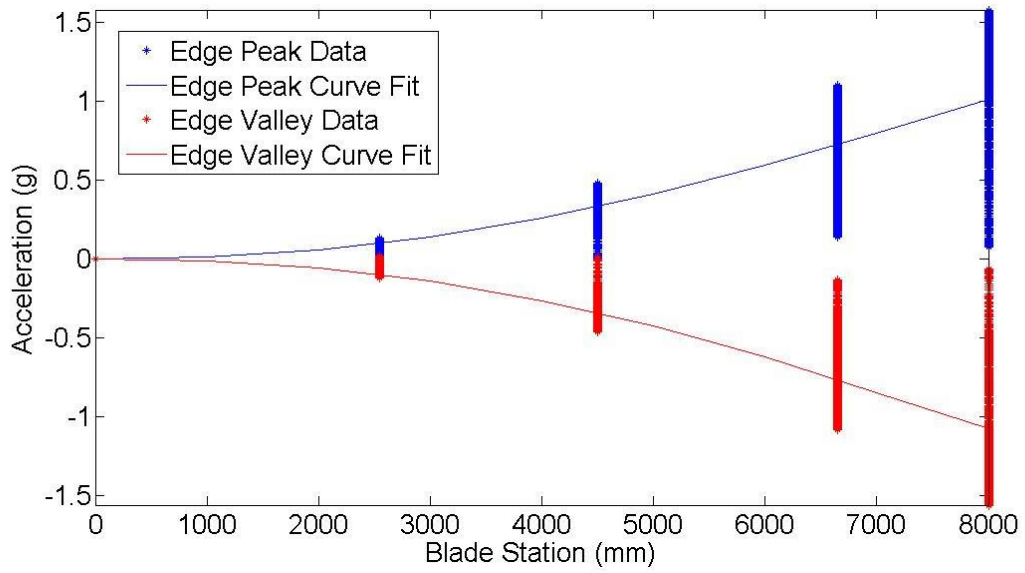
Figure 5.13: Lead-Lag Peak and Valley Deflection Data during Quantum Resonance Test
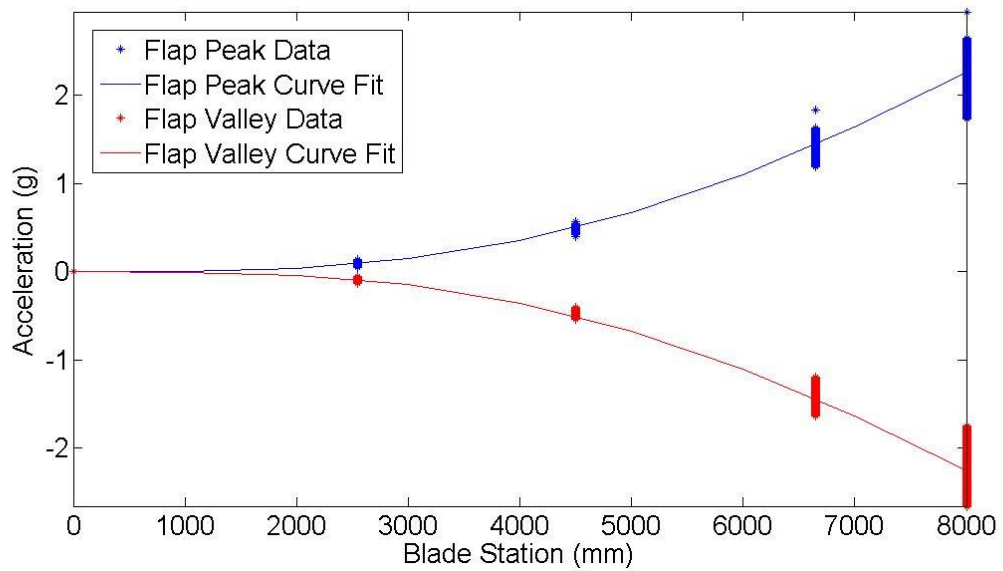
Figure 5.14: Flapwise Peak and Valley Deflection Data during Quantum Resonance Test

The normalized applied moments and target moments for the Quantum Resonance

Test are shown in Figure 5.15 and Figure 5.16.

64
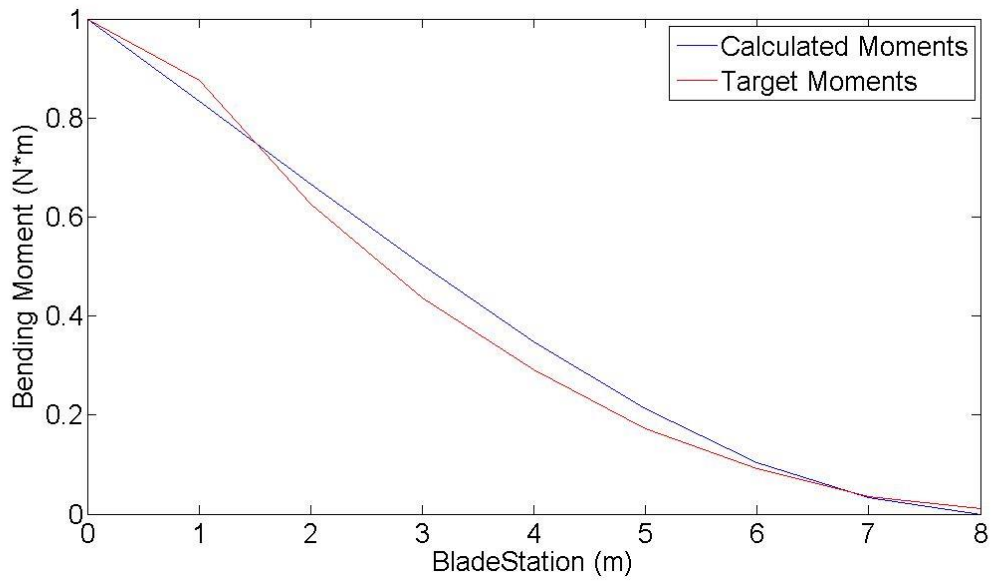
Figure 5.15: Target and Calculated Flapwise Bending Moments during Quantum Test
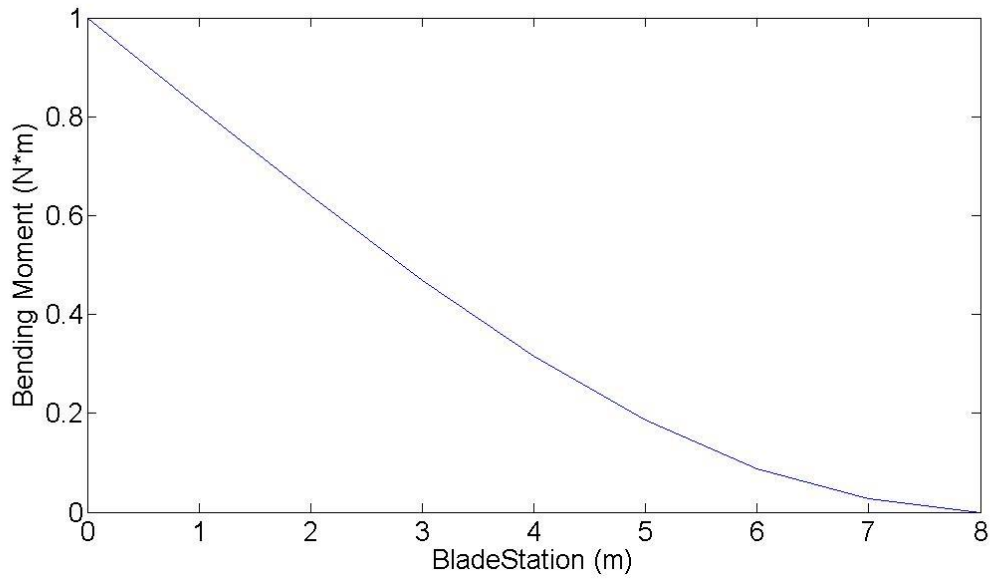
Figure 5.16: Calculated Lead-Lag Bending Moments during Quantum Test

5.3.2   Quantum Resonance Phase Angle

The peak and valley detection of the deflection data is shown in Figure 5.17 and

Figure 5.18.
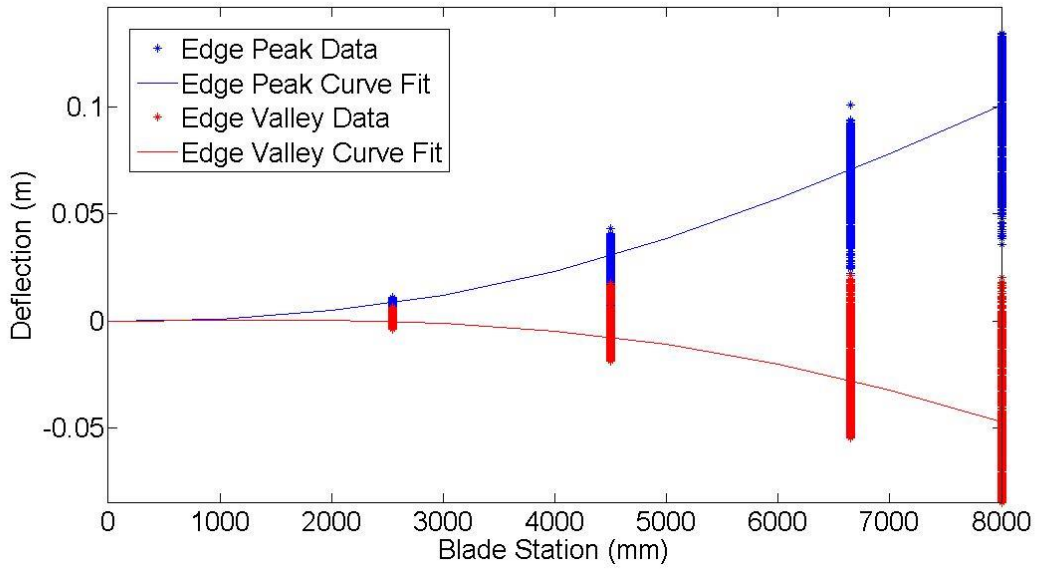
Figure 5.17: Lead-Lag Peak and Valley Deflection Data during Quantum Resonance Test
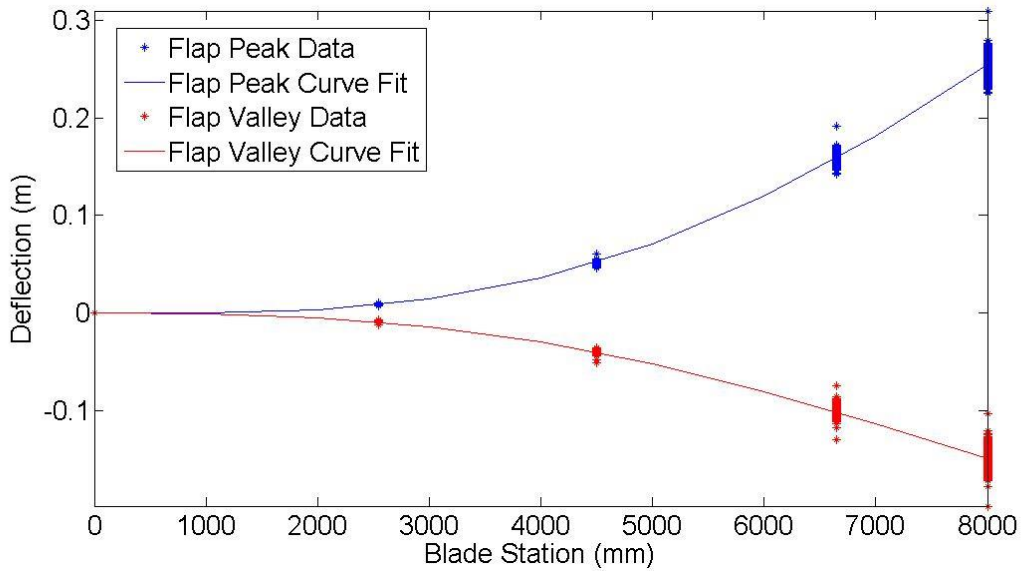
Figure 5.18: Flapwise Peak and Valley Deflection Data during Quantum Resonance Test

The Lissajous figures of the deflection data at each accelerometer location is shown in Figure 5.19. The largest oval is the deflection at the 8000-mm blade station.
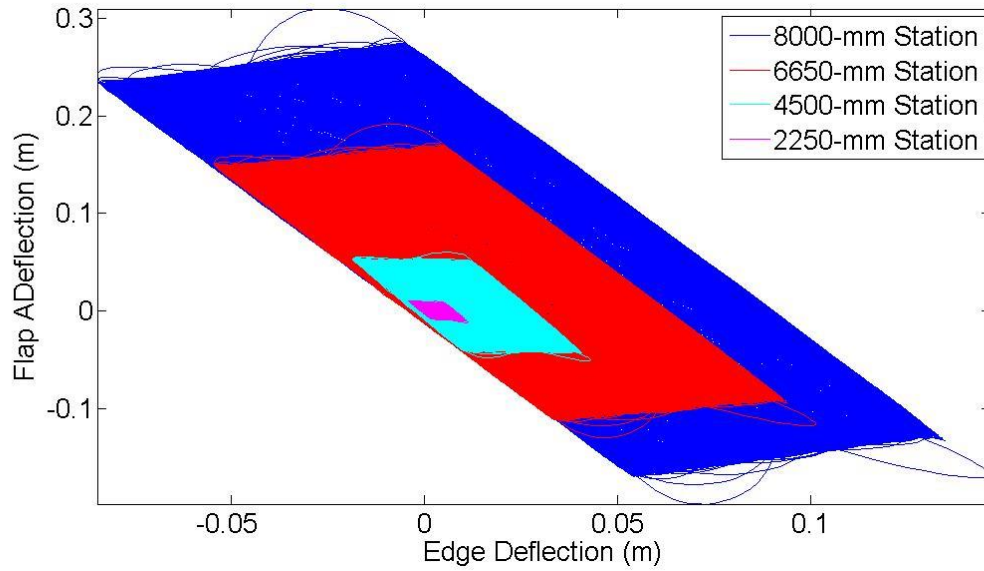
Figure 5.19: Cross-Section of Lead-Lag and Flapwise Deflection Data during Quantum Resonance Test

CHAPTER 6: DISCUSSION OF RESULTS

6.1 Applied Moments

The flapwise bending moments applied during the PhLEX test and quantum resonance test are reproduced in Figure 6.1 and Figure 6.2. Both tests appear to approximate the target bending moments, but neither are exact. The PhLEX test has a percent error of 48-percent at the 5-meter blade station. The quantum resonance test has a percent error of 23-percent at the 5-meter blade station.
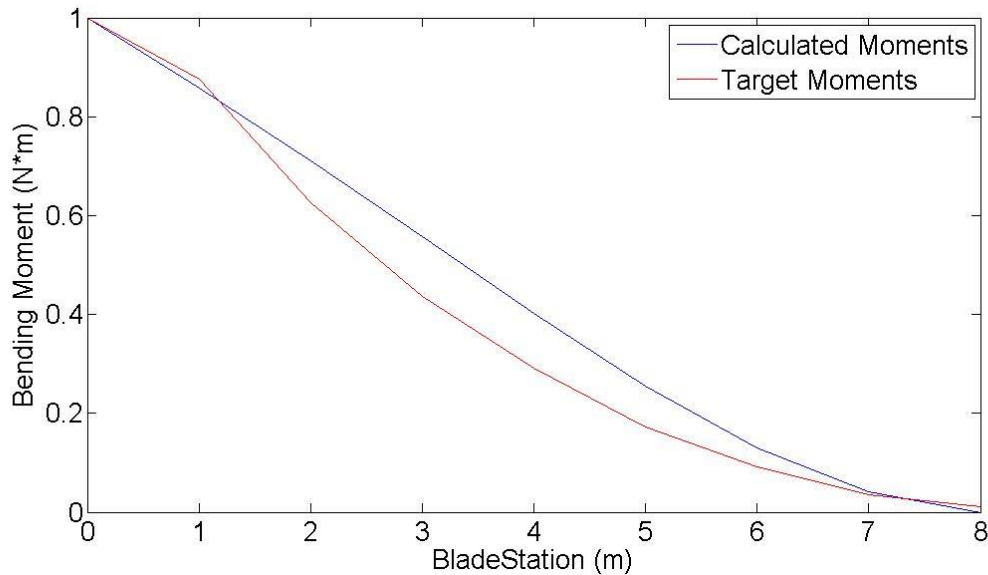
Figure 6.1: Target and Calculated Flapwise Bending Moments during PhLEX Test
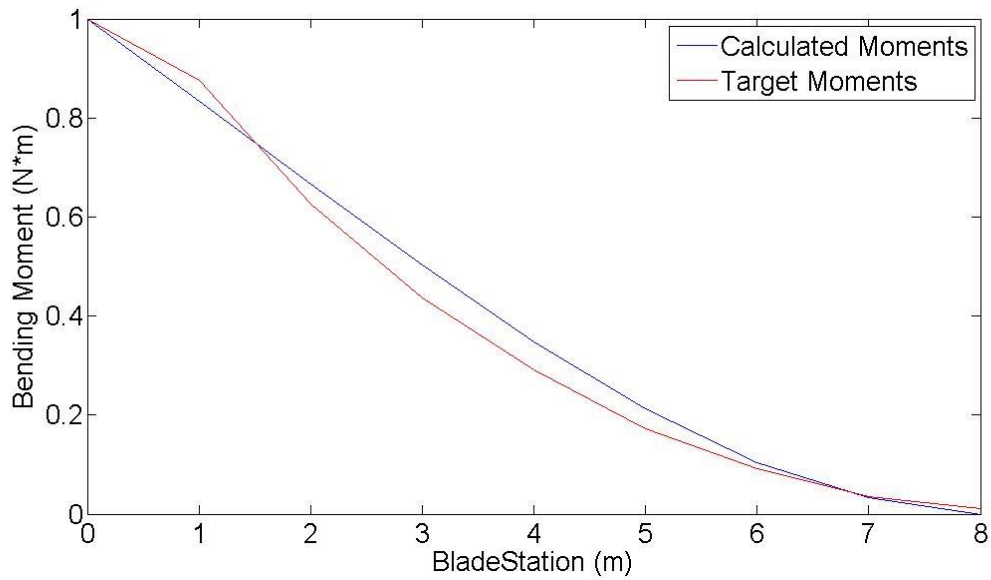
Figure 6.2: Target and Calculated Flapwise Bending Moments during Quantum Test

The moment distributions along the blade can be tuned by optimizing the location of the saddles and adding weights along the blade. As stated earlier, the saddle locations were not optimized for the proof-of-concept test, rather they were selected due to availability of equipment at the 1.6-meter and 6.75-meter blade stations.

6.2   Phase Angle

The Lissajous figures of the PhLEX test and quantum resonance test are reproduced in Figure 6.3 and Figure 6.4.
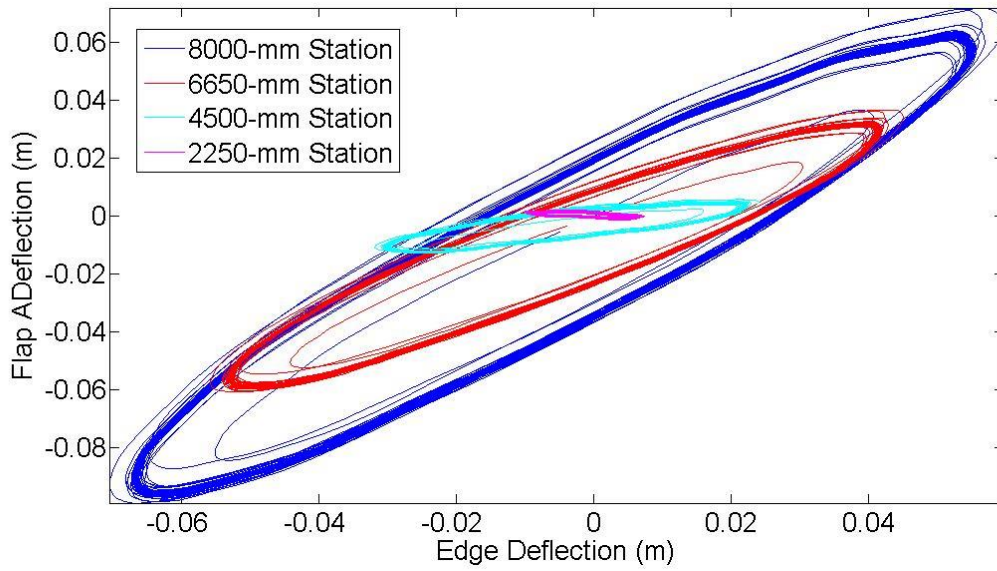
Figure 6.3: Cross-Section of Lead-Lag and Flapwise Deflection Data during PhLEX Test
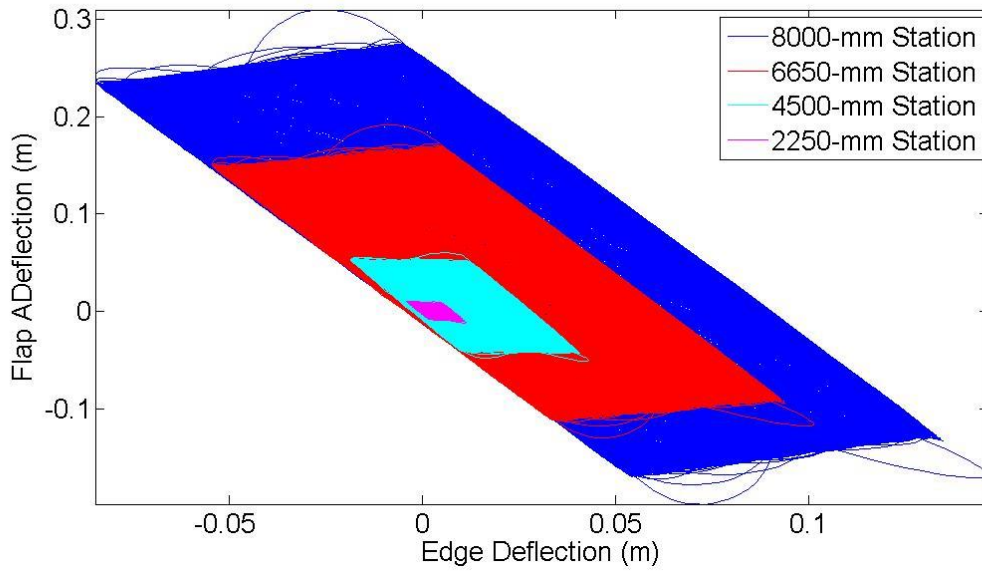
Figure 6.4: Cross-Section of Lead-Lag and Flapwise Deflection Data during Quantum Resonance Test

As can be seen, the PhLEX test is able to produce a repeatable motion every cycle with a constant phase angle. The quantum resonance test is more chaotic. While the

motion of the blade is repeated, the phase angle is not held constant from cycle to cycle. A distribution of the phase angle for the PhLEX test and the quantum resonance test were created using a histogram with 100 bins, as shown in Figure 6.5 and Figure 6.6.
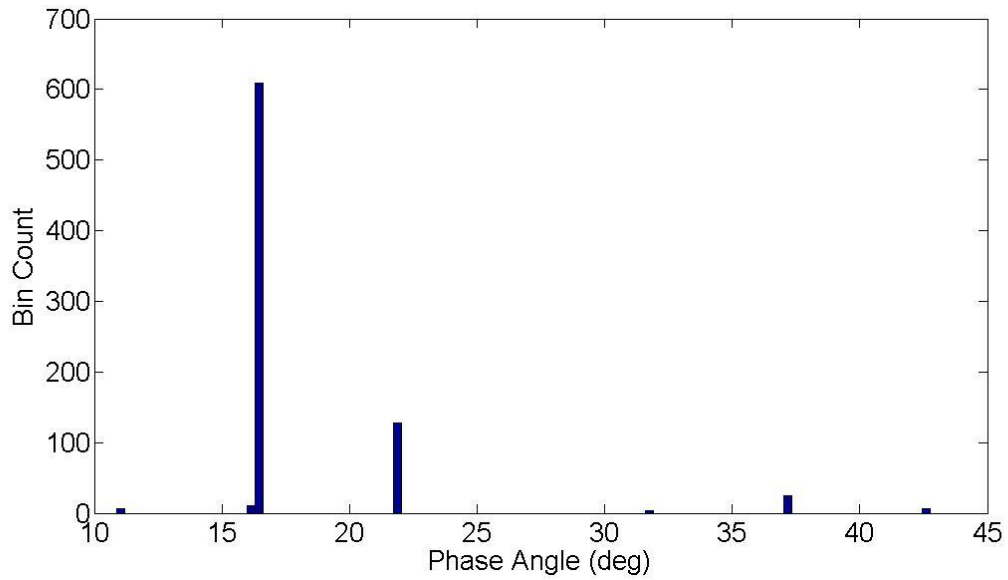
Figure 6.5: Phase Angle Distribution of the PhLEX Test
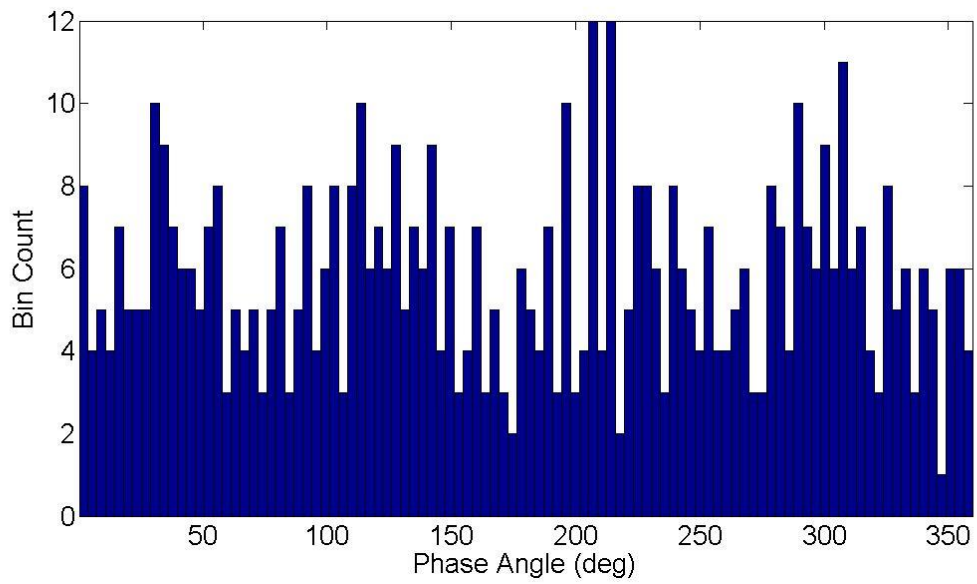
Figure 6.6: Phase Angle Distribution of Quantum Resonance Test

The phase angle distribution of the PhLEX shows a pre-dominate phase angle at 16.5-degrees. The phase angle distribution of the quantum resonance test has a uniform distribution.

CHAPTER 7: CONCLUSIONS

The proof-of-concept test was conducted at the NWTC in 2012 to validate the

control methodology of the dual-axis resonant PhLEX fatigue test system. The

control methodology developed in Phase III was unable to be tested due to

limitations of the software available during the test; however, the PhLEX method

was tested using the control methods available. It was found that a dual-axis

resonant fatigue test, operating at the lead-lag fundamental frequency, was able to

hold a locked phase angle of 16.5-degrees for a total of five thousand cycles at 3-

percent of the target bending moment.

Other key findings of the proof-of-concept test are as follows:

1. Using simple feedback in force control or displacement control on the PhLEX

   actuator was ineffective and caused instability in the system during some

   tests.

2. Using dual compensation control with displacement as the primary feedback

   and load as the secondary feedback on the PHLEX actuator was effective.

3. The current control methodology was unable to filter high frequency

   disturbances

   a. The lead-lag compensator developed in Phase II was implemented to

      filter the disturbance, but proved ineffective.

4. The disturbance is believed to be caused by valve flutter in the PhLEX actuator, and could be eliminated by using a more appropriate actuator or an adaptive spring element.

5. The bending moments approximated the target bending moments.

    a. The moment distribution could be tuned to more closely match the target bending moment distribution by optimizing the test set-up.

CHAPTER 8: FUTURE WORK

The proof-of-concept test successfully proved the ability of the dual-axis resonant PhLEX fatigue test method to control the phase angle during a test performed at the lead-lag fundamental frequency. Possible investigations to move the PhLEX test method into the next stage of development are given below.

1. The test set-up was not optimal for this proof-of-concept test. Optimizing the saddle weights and locations, the PhLEX actuator location, and added masses along the blade can tune the moment distribution to more closely match the target moment distribution.

2. Perform damage analysis on PhLEX proof-of-concept test and compare with other test methods to determine most accurate loading method.

3. Investigate alternatives to the PhLEX actuator used, including different actuator selection (i.e. double-ended actuator, electro-mechanical actuator, multiple hydraulic actuators) or replacing the actuator with a tunable spring element.

4. Investigate control methods to reject disturbances and track phase angle during test that do not require advanced control software.

REFERENCES

[1] R. Hills, "The Horizontal Windmill," in *Power from Wind*. Cambridge, UK: Cambridge Univ. Press, 1994, ch. 2, pp. 11-23.

[2] P. Musgrove, "The First Windmills," in *Wind Power*. Cambridge, UK: Cambridge Univ. Press, 2010, ch. 2, pp. 15-22.

[3] J. F. Manwell, *et.al.,* "Introduction: Modern Wind Energy and Its Origins," in *Wind Energy Explained: Theory, Design, and Application*, 2nd ed. Chicester, UK: J. Wiley, 2009, ch. 1, pp. 1-21.

[4] R. Hills, "The Post Mill," in *Power from Wind*. Cambridge, UK: Cambridge Univ. Press, 1994, ch. 3, pp. 24-51.

[5] P. Musgrove, "Seven Centuries of Service," in *Wind Power*. Cambridge, UK: Cambridge Univ. Press, 2010, ch. 3, pp. 27-52.

[6] R. Hills, "Tower and Smock Mills," in *Power from Wind*. Cambridge, UK: Cambridge Univ. Press, 1994, ch. 4, pp. 51-80.

[7] R. Hills, "The Windmill for Pumping Water and Water Supply," in *Power from Wind*. Cambridge, UK: Cambridge Univ. Press, 1994, ch. 9, pp. 233-264.

[8] P. Musgrove, "Generating Electricity: the Experimental Years, 1887 to 1973," in *Wind Power*. Cambridge, UK: Cambridge Univ. Press, 2010, ch. 4, pp. 57-86.

[9] R. Hills, "Electric Power from Wind," in *Power from Wind*. Cambridge, UK: Cambridge Univ. Press, 1994, ch. 10, pp. 265-282.

[10] "Global Wind Report Annual Market Update 2013," Global Wind Energy Council, Brussels, Belgium, 2013. Available at http://www.gwec.net/publications/global-wind-report-2/.

[11] "Wind Power Factbook," Schlumberger SBC Energy Ins., Gravenhage, Netherlands, 2013. Available at http://www.sbc.slb.com/SBCInstitute/Publications/Wind.aspx.

[12] A. Barr, Blade Technology Trends and Market Updates [online presentation]. Available at http://windworkshops.sandia.gov/agenda/.

[13] "Testing, Manufacturing, and Component Development Projects for Utility-Scale and Distributed Wind Energy," U.S. DOE Energy Efficiency & Renewable Energy, 2014. Available at http://energy.gov/sites/prod/files/2014/05/f15/TestingManufacturingProjectsReport_0.pdf

[14] P. Veers, *et.al.*, "Trends in the Design, Manufacture, and Evaluation of Wind Turbine Blades," *Wind Energy*, vol. 6, no. 3, pp. 245-259, Jun, 2003.

[15] D. White, "New Method for Dual-Axis Fatigue Testing of Large Wind Turbine Blades using Resonance Excitation and Spectral Loading," NREL, Golden, CO, Tech. Rep. TP-500-35268, 2004.

[16] Wind Turbine Generator Systems – Part 23: Full-Scale Structural Testing of Rotor Blades, DS/IEC/TS 61400-23, 2002.

[17] J. F. Manwell, *et.al.,* "Wind Characteristics and Resources," in *Wind Energy Explained: Theory, Design, and Application*, 2nd ed. Chicester, UK: J. Wiley, 2009, ch. 2, pp. 23-87.

[18] A. Rosa, "Wind Energy," in *Fundamentals of Renewable Energy Processes*, 2nd ed. Burlington: Elsevier, 2009, ch. 15, pp. 723-798.

[19] G. Boyle, "Wind Energy," *Renewable Energy Power for a Sustainable Future*, 2nd ed. Oxford, UK: Oxford Univ. Press, 2004, ch. 7, pp. 244-297.

[20] M. Desmond. "The Development of a Wind Turbine Finite Element Model to Predict Loads and Deflections during Static and Fatigue Structural Testing," M.S. thesis, Mech. Eng., ERAU, FL, 2009.

[21] J. F. Manwell, *et.al.,* "Aerodynamics of Wind Turbines," in *Wind Energy Explained: Theory, Design, and Application*, 2nd ed. Chicester, UK: J. Wiley, 2009, ch. 3, pp. 91-155.

[22] P. Hogg. (2010). *Wind Turbine Blade Materials* [online]. Available at http://www.supergen-wind.org.uk/docs/presentations/.

[23] J. F. Manwell, *et.al.,* "Mechanics and Dynamics," in *Wind Energy Explained: Theory, Design, and Application*, 2nd ed. Chicester, UK: J. Wiley, 2009, ch. 4, pp. 157-203.

[24] S. Larwood, *et. al.*, "NedWind 25 Blade Testing at NREL for the European Standards Measurement and Testing Program," NREL, Golden, CO, Tech. Rep. TP-500-29103.

[25] H. Sutherland, "On the Fatigue Analysis of Wind Turbines," SNL, Albuquerque, NM, Tech Rep. SAND99-0089.

[26] D. White, *et. al.*, "Evaluation of the New B-REX Fatigue Testing System for Multi-Megawatt Wind Turbine Blades," NREL, Golden, CO, Tech. Rep. CP-500-37075.

 [27] D. Snowberg, *et. al.*, "Implementation of a Biaxial Resonant Fatigue Test Method on a Large Wind Turbine Blade," NREL, Golden, CO, Tech. Rep. TP-5000-61127.

[28] MTS, "Wind Turbine Blade Testing Solutions," [online]. Available at http://www.mts.com/ucm/groups/public/documents/library/dev_005130.pdf.

[29] P. Malhotra, "Advanced Blade Testing Methods for Wind Turbines," M.S. thesis, Mech. Eng., Univ. Mass Amherst, MA, 2010.

[30] R. S. Court, *et. al.*, "Fatigue Testing of Wind Turbine Blades with Computational Verification," ICCM, Edinburgh, Scotland, 2009.

[31] P. Greaves, "Evaluation of Dual Axis Testing of Wind Turbine Blades," EWEA, Amsterdam, Netherlands, 2011.

[32] P. Greaves, "Fatigue Analysis and Testing of Wind Turbine Blades," Ph.D. dissertation, Eng. And Comp. Sci., Durham Univ., Durham, UK, 2013.

[33] N. Ledford, "Dynamic Analysis of a New Base Excitation Testing System for Fatiguing Wind Turbine Blades," M.S. thesis, Aero. Eng. Sci., Univ. Colo. Boulder, Boulder, CO, 2010.

[34] D. White, *et. al.*, "Development of a Dual-Axis Phase-Locked Resonant Excitation Test Method for Fatigue Testing of Wind Turbine Blades," ASME IMECE, Denver, CO, 2011.

[35] J. Beckwith, *et. al.*, "Development of a Dual-Axis Phase-Locked Excitation (PhLEX) Resonant Fatigue Test Method for Wind Turbine Blades," ASME IMECE, San Diego, CA, 2013.

[36] K. Freeman, "The Development of a Phase-Locked Wind Turbine Blade Finite Element Model to Predict Loads and Deflections during Fatigue Testing," M.S. thesis, Mech. Eng., ERAU, FL, 2010.

[37] W. Haupfear, "The Development of an Adaptive Control System for a Phase-Locked Excitation (PhLEX) Method for Advanced Wind Turbine Blade Fatigue Testing," M.S. thesis, Mech. Eng., ERAU, FL, 2010.

[38] W. Gowhariji, "The Development of a Phase-Locked Excitation Testing Method for Full-Scale Wind Turbine Blades," M.S. thesis, Mech. Eng., ERAU, FL, 2011.

 [39] K. Meierjurgen, "The Development of an Amplitude and Load Phase Angle Adaptive Control System for a Phase-Locked Resonant Excitation (PhLEX) Test

Method for Fatigue Testing of Wind Turbine Blades," M.S. thesis, Mech. Eng., ERAU, FL, 2012.

[40] D. White, *et. al.* "Analysis and Demonstration of Advanced Dual-Axis Test Methods for Wind Turbine Blades," unpublished.

[41] D. Berry, "Design of 9-Meter Carbon-Fiberglass Prototype Blades: CX-100 and TX-100," SNL, Albuquerque, NM, Tech. Rep. SAND2008-4648.

[42] J. Paquette, *et. al.*, "Fatigue Testing of 9 m Caron Fiber Wind Turbine Research Blades," SNL, Albuquerque, NM, Tech. Rep. SAND08-0195C.

[43] J. Paquette, *et. al.*, "Structural Testing of 9 m Carbon Fiber Wind Turbine Research Blades," NREL, Golden, CO, Tech. Rep. CP-500-40985.

[44] S. Hughes, "Blade Testing at NREL's National Wind Technology Center," NREL, Golden, CO, Tech. Rep. PR-500-48898.

[45] W. Cheney, *et. al.*, "Numerical Integration," in *Numerical Mathematics and Computing*, 5th ed. Belmont, CA: Brooks/Cole-Thomson Learning, 2004, ch. 5, pp. 195-227.

[46] Univ. of Mass. Lowell, "Numerical Integration and Differentiation Tutorial," [online]. Available at
http://dynsys.uml.edu/tutorials/Integration_Differentiation/Int-diff_tutorial_011405.pdf

[47] J. Hoffman, *et. al*., "Automatic Calibration of a Motion Capture System Based on Inertial Sensors for Tele-Manipulation," Univ. of Bonn, Bonn, Germany. Available at http://cg.cs.uni-bonn.de/aigaion2root/attachments/hoffmann-2010-roboarm.pdf.

[48] Oreg. St. Univ., "Lissajous Figure," [online]. Available at http://www.physics.orst.edu/~rubin/nacphy/CPapplets/lissajous/Fig2pe.html.

[49] "Lissajous Figures," in *Trigonometry: Book 1* [online]. Available at: http://en.wikibooks.org/wiki/Trigonometry/For_Enthusiasts/Lissajous_Figures.

[50] S. Rao, ''Free Vibration of Single-Degree-of-Freedom Systems", in *Mechanical Engineering*, 5th ed. Upper Saddle River, NJ: Pearson Education Inc., 2011, ch. 2, pp. 124-256.

[51] MTS, "MTS Series 793 Tuning & Calibration," [online]. Available at http://www.mts.com/ucm/groups/public/documents/library/mts_010177.pdf

APPENDIX A: INDIVIDUAL TESTS PERFORMED DURING PROOF-OF-CONCEPT

7/3/2012	Blade Modal Tests	
7/23/2012	Blade with Saddles Modal Tests	
7/24/2012	Blade with Saddles and PhLEX actuator Modal Tests	
	Blade with Saddles and PhLEX actuator Modal Tests, hydraulics attached	
7/25/2012	System Shakedowns:	
	PhLEX actuator only, force control	system went unstable
	PhLEX actuator only, disp control, LC feedback	system stable, seeing clockwise rotation
	adjusted PhLEX actuator angle	
	PhLEX actuator only, dual mode control, accel feedback	seeing disturbance on signal, approx 10X frequency
	PhLEX actuator only, force control	seeing disturbance on signal, approx 10X frequency
	PhLEX actuator only, force control, using PVC P = 4.5, I = 0.0147, D = 0.003, FL = 5 Hz	seeing disturbance on signal, approx 10X frequency
7/26/2012	replaced 1/2 in rubber on PhLEX saddle with 1/4 in rubber	seeing disturbance on signal, approx 10X frequency
	switched polarity of UREX actuators	seeing disturbance on signal, approx 10X frequency
	tested F/F2 gain, P = 5.5, I = 0, D = 0.003, FL = 5 Hz, F/F2 = 0	seeing disturbance on signal, approx 10X frequency
	restored actuator polarities	seeing disturbance on signal, approx 10X frequency
	lead-lag filter on PhLEX force, pole 1,2 = 2.62 Hz, zero 1,2 = 30 Hz	seeing disturbance on signal, approx 10X frequency
	low-pass filter at 3 Hz	seeing disturbance on signal, approx 10X frequency

7/27/2012	removed UREX actuators from saddle	seeing disturbance on signal, approx 10X frequency
7/31/2012	designed vibration absorber	seeing disturbance on signal, approx 10X frequency
8/1/2012	modified vibration absorber	seeing disturbance on signal, approx 10X frequency
	removed vibration absorber	
	run Edge UREX and PhLEX at edge fund. freq., 1.85g in flap, 0.34g in edge	dist. still present, seeing very little edge motion
	run Edge UREX and PhLEX at 3.84 Hz, 1.85g in flap, 0.34g in edge, monitoring 66500-mm accel	dist. still present, seeing very little edge motion, 1 g flap, 200 mg edge
	run Edge UREX and PhLEX at 3.03 Hz w/ 72-deg phase lag of PhLEX, both in MPT	seeing more edge motion, 1.6 g flap, 400 mg edge
	run Edge UREX and PhLEX at 3.03 Hz w/ 72-deg phase lag of PhLEX, both in MPT, vib. abs. in UREX saddle	increased dist. Signal spikes
8/2/2012	attached UREX actuators	
	ran single-axis tests w/ UREX	lead-lag = 2.61 Hz, flap = 2.63 Hz
8/3/2012	run Edge and Flap UREX at edge fund 2.63 Hz w/ 72-deg phase lag in Edge	
	run all actuators at edge fund. 2.63 Hz w/ Edge and Flap UREX at -18-deg phase lag	excited a higher order around 51 Hz, system became unstable
	tuned disp. Control of PhLEX	dist. at peaks of PhLEX LVDT
	PhLEX in force control	system unstable
	vary phase lag of UREX actuators	cannot achieve 90-deg phase angle
	run only PhLEX in MPT	unstable
	run PhLEX in disp. control w/ Edge UREX in 90-deg phase lag	dist. still present, cannot achieve 90-deg phase angle
	180-deg phase lag	dist. still present, cannot achieve 90-deg phase angle

8/7/2012	dual mode force control, PhLEX in disp. control w/ LC feedback, 2.61 Hz	
	adjusted actuator angle to 1-deg	system unstable
	removed D gain, P = 2.25, I = 0.50, FL = 10 Hz, int. limit = 10%	stable, clockwise, dual axis motion
	introduced Edge UREX, P = 1.02, I = 0.005, FL = 10 Hz	stable, +/- 3 in, PhLEX +/- 1.5 in
	perform frequency sweep	

APPENDIX B: MATLAB SCRIPTS

Main Script

```matlab
%% Description
%
% Purpose: Data analysis of PhLEX Proof of Concept Test (Accel Signals)
%
% Created By: J. Beckwith
% Date: 11/19/2014
% Last Update: 11/21/2014
%
%% Initialize
clear all; close all; clc
% define varibales
Fs = 200; % sampling frequency
%file_name =
'PhLEX+EdgeBasicDualModeForce_2012_08_07_17_36_48_200Hz.xls'; % PhLEX
File
file_name = 'Dual-axis UREX actuators_2012_08_02_14_55_40_200Hz.xls'; %
UREX file

%% Read in Data

% read files
data = xlsread(file_name,2,'A2:S60001');
% organize data into signal types
TimeStamp = data(:,1);
PhLEXLoadCell = data(:,6);
LVDT = data(:,7:10);
EdgeAccels = data(:,12:2:18);
FlapAccels = data(:,11:2:17);
StrainG = data(:,19);

% center data
for i = 1:4
    EdgeAccels(:,i) = EdgeAccels(:,i) - mean(EdgeAccels(:,i));
    FlapAccels(:,i) = FlapAccels(:,i) - mean(FlapAccels(:,i));
    LVDT(:,i) = LVDT(:,i) - mean(LVDT(:,i));
end

% adjust time
TimeStamp = (TimeStamp - TimeStamp(1)) * 10^5;

%% Select Plots
% 1 = plot, 0 = do not plot
% plot single-sided amplitude spectrum of accels signals
plotFFT = 0;
% plot peak/valley detection for each accel signal
plotpvdet = 0;
```

86

```matlab
% plot curve fit to accel peaks and accel peaks
plotcurve = 1;
% plot signals
plotsig = 0;
% plot phase angle
plotphase = 0;

%% Determine Excitation Frequency
[freq_E,freq_F] = PlotFFT(plotFFT,Fs,EdgeAccels,FlapAccels);

%% Filter Data (Low-Pass Butterworth Filter w/ 10 Hz cut-off freq)
% select to filter data
filtering = 0; % 1 = yes, 0 = no
% call function
if filtering == 1
[EdgeAccels,FlapAccels,PhLEXLoadCell] = Bfilter(Fs,EdgeAccels,...
    FlapAccels,PhLEXLoadCell);
end
%% Peak & Valley Detection of Accel Data
[EdgePeakAccel,EdgePeakTime,EdgeValleyAccel,EdgeValleyTime,FlapPeakAcce
l...
    ,FlapPeakTime,FlapValleyAccel,FlapValleyTime] = pvdet(plotpvdet,...
    freq_E,freq_F,Fs,TimeStamp,EdgeAccels,FlapAccels);

%% Curve Fit Data
% select accel to use as reference for creating data sets
ai = 3;
% select how many points to use in graphing curve fit
pts = 10;
% call function
[t,poly_Ep,poly_Ev,poly_Fp,poly_Fv] = CurveFit(plotcurve,ai,pts,...
    EdgePeakAccel,EdgeValleyAccel,FlapPeakAccel,FlapValleyAccel);

%% Plots
% plot signals
if plotsig == 1
    figure
    plot(TimeStamp(5000:5999),EdgeAccels(5000:5999,:))
    xlabel('Time')
    ylabel('Edge Accelerometer Signals (g)')
    legend('2250','4500','6650','8000')
    axis tight
    figure
    plot(TimeStamp(5000:5999),FlapAccels(5000:5999,:))
    xlabel('Time')
    ylabel('Flap Accelerometer Signals (g)')
    legend('2250','4500','6650','8000')
    axis tight
    figure
    plot(TimeStamp(5000:5999),LVDT(5000:5999,:))
    xlabel('Time')
    ylabel('LVDT Signals (in)')
```

```matlab
    legend('North UREX','South UREX','Edge UREX','PhLEX')
    axis tight
    figure
    plot(TimeStamp(5000:5999),PhLEXLoadCell(5000:5999))
    xlabel('Time')
    ylabel('PhLEX Load Cell (lbs)')
    axis tight
    figure
    plot(TimeStamp(5000:5999),StrainG(5000:5999))
    xlabel('Time')
    ylabel('Strain Gauge (in/in)')
    axis tight
end

% plot phase angle
if plotphase == 1
    figure
    plot(EdgeAccels(:,3),FlapAccels(:,3))
    xlabel('Edge Acceleration (g)')
    ylabel('Flap Acceleration (g)')
    axis tight
    figure
    plot(EdgeAccels(:,4),FlapAccels(:,4),'b');hold on
    plot(EdgeAccels(:,3),FlapAccels(:,3),'r');hold on
    plot(EdgeAccels(:,2),FlapAccels(:,2),'c');hold on
    plot(EdgeAccels(:,1),FlapAccels(:,1),'m');
    xlabel('Edge Acceleration (g)')
    ylabel('Flap Acceleration (g)')
    legend('8000','6650','4500','2250')
    axis tight
end
```

PlotFFT Function

```matlab
function[freq_E,freq_F] = PlotFFT(plotFFT,Fs,EdgeAccels,FlapAccels)
%% Description
%
% Purpose: This function determines the frequnecy at which the test was
performed and plots the single-sided amplitude spectrum of y(t).
%
% Created By: J. Beckwith
% Date: 11/19/2014
%
%% Initialize
% define variables
L = length(EdgeAccels);
NFFT = 2^nextpow2(L);
f = Fs/2*linspace(0,1,NFFT/2+1);

%% Take FFT of Signals
for i = 1:4
```

```matlab
    E_Y(:,i) = fft(EdgeAccels(:,i),NFFT)/L;
    F_Y(:,i) = fft(FlapAccels(:,i),NFFT)/L;
end

%% Determine Excitation Frequnecy
% find indice where f > 10 Hz
f_10 = find(f>10);
% find max power for each accelerometer
for i = 1:4
    [pk_E(i),pkloc_E(i)] = max(2*abs(E_Y(1:f_10(1),i)));
    [pk_F(i),pkloc_F(i)] = max(2*abs(F_Y(1:f_10(1),i)));
end
% find corresponding frequency (assumes all frequencies are at same
indice)
freq_E = f(pkloc_E(1));
freq_F = f(pkloc_F(1));

%% Plots
if plotFFT == 1;
    % edge accels
    figure
    semilogy(f(2:end),2*abs(E_Y(2:NFFT/2+1,1)))
    title('Single-Sided Amplitude Spectrum of Edge 2550-mm Accel')
    xlabel('Frequency (Hz)')
    ylabel('|Y(f)|')

    figure
    semilogy(f(2:end),2*abs(E_Y(2:NFFT/2+1,2)))
    title('Single-Sided Amplitude Spectrum of Edge 4500-mm Accel')
    xlabel('Frequency (Hz)')
    ylabel('|Y(f)|')

    figure
    semilogy(f(2:end),2*abs(E_Y(2:NFFT/2+1,3)))
    title('Single-Sided Amplitude Spectrum of Edge 6650-mm Accel')
    xlabel('Frequency (Hz)')
    ylabel('|Y(f)|')

    figure
    semilogy(f(2:end),2*abs(E_Y(2:NFFT/2+1,4)))
    title('Single-Sided Amplitude Spectrum of Edge 8000-mm Accel')
    xlabel('Frequency (Hz)')
    ylabel('|Y(f)|')
    % flap accels
    figure
    semilogy(f(2:end),2*abs(F_Y(2:NFFT/2+1,1)))
    title('Single-Sided Amplitude Spectrum of Flap 2250-mm Accel')
    xlabel('Frequency (Hz)')
    ylabel('|Y(f)|')

    figure
    semilogy(f(2:end),2*abs(F_Y(2:NFFT/2+1,2)))
```

```matlab
    title('Single-Sided Amplitude Spectrum of Flap 4500-mm Accel')
    xlabel('Frequency (Hz)')
    ylabel('|Y(f)|')

    figure
    semilogy(f(2:end),2*abs(F_Y(2:NFFT/2+1,3)))
    %title('Single-Sided Amplitude Spectrum of Flap 6650-mm Accel')
    xlabel('Frequency (Hz)')
    ylabel('|Y(f)|')

    figure
    semilogy(f(2:end),2*abs(F_Y(2:NFFT/2+1,4)))
    title('Single-Sided Amplitude Spectrum of Flap 8000-mm Accel')
    xlabel('Frequency (Hz)')
    ylabel('|Y(f)|')
end
```

Butterworth Filter

```matlab
function[EdgeAccels,FlapAccels,PhLEXLoadCell] =
Bfilter(Fs,EdgeAccels,FlapAccels,PhLEXLoadCell)
%% Description
%
% Purpose: This function filters the accelerometer data with a low-pass
% Butterworth filter with a 10 Hz cut-off frequency.
%
% Created By: J. Beckwith
% Date: 11/19/2014
%
%% Iniitialize
% define variables
L = length(EdgeAccels);
NFFT = 2^nextpow2(L);
f = Fs/2*linspace(0,1,NFFT/2+1);

%% Filter Data
% define indicies for filter
l = ceil(10/(f(2)-f(1)));
h = L - (l-1);

% Take FFT
F1 = fft(EdgeAccels(:,1));
F2 = fft(EdgeAccels(:,2));
F3 = fft(EdgeAccels(:,3));
F4 = fft(EdgeAccels(:,4));
F5 = fft(FlapAccels(:,1));
F6 = fft(FlapAccels(:,2));
F7 = fft(FlapAccels(:,3));
F8 = fft(FlapAccels(:,4));
F9 = fft(PhLEXLoadCell);
% filter
F1(l:h) = 0;
```

```matlab
F2(l:h) = 0;
F3(l:h) = 0;
F4(l:h) = 0;
F5(l:h) = 0;
F6(l:h) = 0;
F7(l:h) = 0;
F8(l:h) = 0;
F9(l:h) = 0;
% declare variables
EdgeAccels(:,1) = ifft(F1,'symmetric');
EdgeAccels(:,2) = ifft(F2,'symmetric');
EdgeAccels(:,3) = ifft(F3,'symmetric');
EdgeAccels(:,4) = ifft(F4,'symmetric');
FlapAccels(:,1) = ifft(F5,'symmetric');
FlapAccels(:,2) = ifft(F6,'symmetric');
FlapAccels(:,3) = ifft(F7,'symmetric');
FlapAccels(:,4) = ifft(F8,'symmetric');
PhLEXLoadCell = ifft(F9,'symmetric');
```

Peak/Valley Detection

```matlab
function
[EdgePeakAccel,EdgePeakTime,EdgeValleyAccel,EdgeValleyTime,FlapPeakAcce
l...
    ,FlapPeakTime,FlapValleyAccel,FlapValleyTime] = pvdet(plotpvdet,...
    freq_E,freq_F,Fs,TimeStamp,EdgeAccels,FlapAccels)
%% Description
% Purpose: Determines peaks and valleys of accel data.
%
% Created By: J. Beckwith
% Date: 11/19/2014

%% Initialize
% define variables
p_E = floor((1 / freq_E) / (1/Fs));
p_F = floor((1 / freq_F) / (1/Fs));

%% Peak Valley Detection of Accel Signals
j(1) = 1;
for k = 1:4
    for i = 1:floor((length(EdgeAccels))/p_E)
        [EdgePeak(i,1,k),EdgePeak(i,2,k)] =
max(EdgeAccels(j(i):(j(i)+...
            (p_E-1)),k));
        [EdgeValley(i,1,k),EdgeValley(i,2,k)] =
min(EdgeAccels(j(i):(j(i)+...
            (p_E-1)),k));
        j(i+1) = j(i) + p_E;
    end
end

j(1) = 1;
```

```matlab
for k = 1:4
    for i = 1:floor((length(FlapAccels))/p_F)
        [FlapPeak(i,1,k),FlapPeak(i,2,k)] =
max(FlapAccels(j(i):(j(i)+...
            (p_F-1)),k));
        [FlapValley(i,1,k),FlapValley(i,2,k)] = min(FlapAccels(j(i):...
            (j(i)+(p_F-1)),k));
        j(i+1) = j(i) + p_F;
    end
end

%% Determine Indicies of Data
for k = 1:4
    for i = 1:length(EdgeValley)
        EdgePeak(i,3,k) = EdgePeak(i,2,k) + (p_E * (i - 1));
        EdgeValley(i,3,k) = EdgeValley(i,2,k) + (p_E * (i - 1));
    end
end

for k = 1:4
    for i = 1:length(FlapValley)
        FlapPeak(i,3,k) = FlapPeak(i,2,k) + (p_F * (i - 1));
        FlapValley(i,3,k) = FlapValley(i,2,k) + (p_F * (i - 1));
    end
end

%% Determine Acceleration of Blade at Peak/Valley Points
for k = 1:4
    for i = 1:length(EdgeValley)
        EdgePeakAccel(i,1:4,k) = EdgeAccels(EdgePeak(i,3,k),:);
        EdgePeakTime(i,1,k) = TimeStamp(EdgePeak(i,3,k));
        EdgeValleyAccel(i,1:4,k) = EdgeAccels(EdgeValley(i,3,k),:);
        EdgeValleyTime(i,1,k) = TimeStamp(EdgeValley(i,3,k));
    end
end

for k = 1:4
    for i = 1:length(FlapValley)
        FlapPeakAccel(i,1:4,k) = FlapAccels(FlapPeak(i,3,k),:);
        FlapPeakTime(i,1,k) = TimeStamp(FlapPeak(i,3,k));
        FlapValleyAccel(i,1:4,k) = FlapAccels(FlapValley(i,3,k),:);
        FlapValleyTime(i,1,k) = TimeStamp(FlapValley(i,3,k));
    end
end

%% Plot Peak/Valley Detection for each Accel
if plotpvdet == 1;
    figure
    plot(TimeStamp,EdgeAccels(:,4)); hold on
    plot(EdgePeakTime(:,1,4),EdgePeak(:,1,4),'r*'); hold on
    plot(EdgeValleyTime(:,1,4),EdgeValley(:,1,4),'g*')
    xlabel('Time')
```

```matlab
    ylabel('8000-mm Edge Accelerometer')
    axis tight
    figure
    plot(TimeStamp,FlapAccels(:,4)); hold on
    plot(FlapPeakTime(:,1,4),FlapPeak(:,1,4),'r*'); hold on
    plot(FlapValleyTime(:,1,4),FlapValley(:,1,4),'g*')
    xlabel('Time')
    ylabel('8000-mm Flap Accelerometer')
    axis tight
    figure
    plot(TimeStamp,EdgeAccels(:,3)); hold on
    plot(EdgePeakTime(:,1,3),EdgePeak(:,1,3),'r*'); hold on
    plot(EdgeValleyTime(:,1,3),EdgeValley(:,1,3),'g*')
    xlabel('Time')
    ylabel('6650-mm Edge Accelerometer')
    axis tight
    figure
    plot(TimeStamp,FlapAccels(:,3)); hold on
    plot(FlapPeakTime(:,1,3),FlapPeak(:,1,3),'r*'); hold on
    plot(FlapValleyTime(:,1,3),FlapValley(:,1,3),'g*')
    xlabel('Time')
    ylabel('6650-mm Flap Accelerometer')
    axis tight
    figure
    plot(TimeStamp,EdgeAccels(:,2)); hold on
    plot(EdgePeakTime(:,1,2),EdgePeak(:,1,2),'r*'); hold on
    plot(EdgeValleyTime(:,1,2),EdgeValley(:,1,2),'g*')
    xlabel('Time')
    ylabel('4500-mm Edge Accelerometer')
    axis tight
    figure
    plot(TimeStamp,FlapAccels(:,2)); hold on
    plot(FlapPeakTime(:,1,2),FlapPeak(:,1,2),'r*'); hold on
    plot(FlapValleyTime(:,1,2),FlapValley(:,1,2),'g*')
    xlabel('Time')
    ylabel('4500-mm Flap Accelerometer')
    axis tight
    figure
    plot(TimeStamp,EdgeAccels(:,1)); hold on
    plot(EdgePeakTime(:,1,1),EdgePeak(:,1,1),'r*'); hold on
    plot(EdgeValleyTime(:,1,1),EdgeValley(:,1,1),'g*')
    xlabel('Time')
    ylabel('2250-mm Edge Accelerometer')
    axis tight
    figure
    plot(TimeStamp,FlapAccels(:,1)); hold on
    plot(FlapPeakTime(:,1,1),FlapPeak(:,1,1),'r*'); hold on
    plot(FlapValleyTime(:,1,1),FlapValley(:,1,1),'g*')
    xlabel('Time')
    ylabel('2250-mm Flap Accelerometer')
    axis tight
end
```

Curve fit Polynomial to Data

```matlab
function[t,poly_Ep,poly_Ev,poly_Fp,poly_Fv] =
CurveFit(plotcurve,ai,pts,EdgePeakAccel,EdgeValleyAccel,FlapPeakAccel,F
lapValleyAccel)
%% Description
%
% Purpose:
%
% Created By: J. Beckwith
% Date: 11/19/14
%
%% Create Acceleration Data Sets
% create blade station data set
xdata_E = [];
for i = 1:length(EdgePeakAccel)
    xdata_E = [xdata_E,0,2550,4500,6650,8000];
end
xdata_F = [];
for i = 1:length(FlapPeakAccel)
    xdata_F = [xdata_F,0,2550,4500,6650,8000];
end
% create acceleration data sets, third indicie determines what accel to
use
% as reference
ydata_EdgePeak = [];
for i = 1:length(EdgePeakAccel)
    ydata_EdgePeak = [ydata_EdgePeak,0,EdgePeakAccel(i,1:4,ai)];
end

ydata_EdgeValley = [];
for i = 1:length(EdgeValleyAccel)
    ydata_EdgeValley = [ydata_EdgeValley,0,EdgeValleyAccel(i,1:4,ai)];
end

ydata_FlapPeak = [];
for i = 1:length(FlapPeakAccel)
    ydata_FlapPeak = [ydata_FlapPeak,0,FlapPeakAccel(i,1:4,ai)];
end

ydata_FlapValley = [];
for i = 1:length(FlapValleyAccel)
    ydata_FlapValley = [ydata_FlapValley,0,FlapValleyAccel(i,1:4,ai)];
end

%% Curve Fit Data to Sixth Degree Polynomial Using Least Squares Method
% curve fit edge accels
% peak data
x0_edge = [1e-15;1e-20;1e-20];
[x_Ep,resnorm_Ep] =
lsqcurvefit(@myfun_edge,x0_edge,xdata_E,ydata_EdgePeak);
```

```matlab
% valley data
x0_edge = [1e-15;1e-20;1e-20];
[x_Ev,resnorm_Ev] =
lsqcurvefit(@myfun_edge,x0_edge,xdata_E,ydata_EdgeValley);

% curve fit flap accels
% peak data
x0_flap = [1e-10;1e-10;1e-10];
[x_Fp,resnorm_Fp] =
lsqcurvefit(@myfun_flap,x0_flap,xdata_F,ydata_FlapPeak);
% valley data
x0_flap = [1e-10;1e-10;1e-10];
[x_Fv,resnorm_Fv] =
lsqcurvefit(@myfun_flap,x0_flap,xdata_F,ydata_FlapValley);

%% Evaluate Ploynomials
[t,poly_Ep,poly_Ev,poly_Fp,poly_Fv] =
evalpoly(pts,x_Ep,x_Ev,x_Fp,x_Fv);

%% Plots
if plotcurve == 1
    figure
    plot(xdata_E,ydata_EdgePeak,'b*'); hold on
    plot(t,poly_Ep,'b'); hold on
    plot(xdata_E,ydata_EdgeValley,'r*'); hold on
    plot(t,poly_Ev,'r')
    xlabel('Blade Station (mm)')
    ylabel('Acceleration (g)')
    legend('Edge Peak Data','Edge Peak Curve Fit','Edge Valley
Data','Edge Valley Curve Fit')
    axis tight

    figure
    plot(xdata_F,ydata_FlapPeak,'b*'); hold on
    plot(t,poly_Fp,'b'); hold on
    plot(xdata_F,ydata_FlapValley,'r*'); hold on
    plot(t,poly_Fv,'r')
    xlabel('Blade Station (mm)')
    ylabel('Acceleration (g)')
    legend('Flap Peak Data','Flap Peak Curve Fit','Flap Valley
Data','Flap Valley Curve Fit')
    axis tight
end
```

Integrate Acceleration to Deflection

```matlab
function [outputs] = integratedata(inputs)
%% Description
%
% Purpose: This script integrates discrete data sets. (This script is
% currently written exclusively for accel signal from PhLEX POC test)
%
```

```matlab
% Created By: J. Beckwith
% Date: 11/19/2014
% Last Updated: 11/21/2014
%

%% Integration to Velocity using Trapezoidal Rule
% convert gs to m/s^2
EdgeAccels_mod = 9.81 * EdgeAccels;
FlapAccels_mod = 9.81 * FlapAccels;

% define first integration step
% edge
EdgeVels(1,1) = 0.5 * (TimeStamp(2) - TimeStamp(1)) *
(EdgeAccels_mod(1,1) + EdgeAccels_mod(2,1));
EdgeVels(1,2) = 0.5 * (TimeStamp(2) - TimeStamp(1)) *
(EdgeAccels_mod(1,2) + EdgeAccels_mod(2,2));
EdgeVels(1,3) = 0.5 * (TimeStamp(2) - TimeStamp(1)) *
(EdgeAccels_mod(1,3) + EdgeAccels_mod(2,3));
EdgeVels(1,4) = 0.5 * (TimeStamp(2) - TimeStamp(1)) *
(EdgeAccels_mod(1,4) + EdgeAccels_mod(2,4));
% flap
FlapVels(1,1) = 0.5 * (TimeStamp(2) - TimeStamp(1)) *
(FlapAccels_mod(1,1) + FlapAccels_mod(2,1));
FlapVels(1,2) = 0.5 * (TimeStamp(2) - TimeStamp(1)) *
(FlapAccels_mod(1,2) + FlapAccels_mod(2,2));
FlapVels(1,3) = 0.5 * (TimeStamp(2) - TimeStamp(1)) *
(FlapAccels_mod(1,3) + FlapAccels_mod(2,3));
FlapVels(1,4) = 0.5 * (TimeStamp(2) - TimeStamp(1)) *
(FlapAccels_mod(1,4) + FlapAccels_mod(2,4));

% integrate data
for i = 1:length(EdgeAccels_mod)-1
    % edge
    EdgeVels(i+1,1) = EdgeVels(i,1) + 0.5 * (TimeStamp(i+1) -
TimeStamp(i)) * (EdgeAccels_mod(i,1) + EdgeAccels_mod(i+1,1));% +
((7*10^-5) * (1/Fs));
    EdgeVels(i+1,2) = EdgeVels(i,2) + 0.5 * (TimeStamp(i+1) -
TimeStamp(i)) * (EdgeAccels_mod(i,2) + EdgeAccels_mod(i+1,2));% +
(0.0004 * (1/Fs));
    EdgeVels(i+1,3) = EdgeVels(i,3) + 0.5 * (TimeStamp(i+1) -
TimeStamp(i)) * (EdgeAccels_mod(i,3) + EdgeAccels_mod(i+1,3));% +
(0.0009 * (1/Fs));
    EdgeVels(i+1,4) = EdgeVels(i,4) + 0.5 * (TimeStamp(i+1) -
TimeStamp(i)) * (EdgeAccels_mod(i,4) + EdgeAccels_mod(i+1,4));% +
(0.0013 * (1/Fs));
    % flap
    FlapVels(i+1,1) = FlapVels(i,1) + 0.5 * (TimeStamp(i+1) -
TimeStamp(i)) * (FlapAccels_mod(i,1) + FlapAccels_mod(i+1,1));% +
(0.0002 * (1/Fs));
    FlapVels(i+1,2) = FlapVels(i,2) + 0.5 * (TimeStamp(i+1) -
TimeStamp(i)) * (FlapAccels_mod(i,2) + FlapAccels_mod(i+1,2));% +
((6*10^-5) * (1/Fs));
```

```
    FlapVels(i+1,3) = FlapVels(i,3) + 0.5 * (TimeStamp(i+1) -
TimeStamp(i)) * (FlapAccels_mod(i,3) + FlapAccels_mod(i+1,3));% +
(0.0002 * (1/Fs));
    FlapVels(i+1,4) = FlapVels(i,4) + 0.5 * (TimeStamp(i+1) -
TimeStamp(i)) * (FlapAccels_mod(i,4) + FlapAccels_mod(i+1,4));% +
(0.0004 * (1/Fs));
end

%% Filter Data (High-Pass Butterworth Filter w/ 1 Hz cut-off freq)
[EdgeVels_f,FlapVels_f] = Bfilter_vel(Fs,EdgeVels,FlapVels);

% EdgeVels_f = EdgeVels;
% FlapVels_f = FlapVels;
%% Integration to Deflection using Trapezoidal Rule
% define first integration step
% edge
EdgeDefs(1,1) = 0.5 * (TimeStamp(2) - TimeStamp(1)) * (EdgeVels_f(1,1)
+ EdgeVels_f(2,1));
EdgeDefs(1,2) = 0.5 * (TimeStamp(2) - TimeStamp(1)) * (EdgeVels_f(1,2)
+ EdgeVels_f(2,2));
EdgeDefs(1,3) = 0.5 * (TimeStamp(2) - TimeStamp(1)) * (EdgeVels_f(1,3)
+ EdgeVels_f(2,3));
EdgeDefs(1,4) = 0.5 * (TimeStamp(2) - TimeStamp(1)) * (EdgeVels_f(1,4)
+ EdgeVels_f(2,4));
% flap
FlapDefs(1,1) = 0.5 * (TimeStamp(2) - TimeStamp(1)) * (FlapVels_f(1,1)
+ FlapVels_f(2,1));
FlapDefs(1,2) = 0.5 * (TimeStamp(2) - TimeStamp(1)) * (FlapVels_f(1,2)
+ FlapVels_f(2,2));
FlapDefs(1,3) = 0.5 * (TimeStamp(2) - TimeStamp(1)) * (FlapVels_f(1,3)
+ FlapVels_f(2,3));
FlapDefs(1,4) = 0.5 * (TimeStamp(2) - TimeStamp(1)) * (FlapVels_f(1,4)
+ FlapVels_f(2,4));

% integrate data
for i = 1:length(EdgeVels)-1
    % edge
    EdgeDefs(i+1,1) = EdgeDefs(i,1) + 0.5 * (TimeStamp(i+1) -
TimeStamp(i)) * (EdgeVels_f(i,1) + EdgeVels_f(i+1,1));
    EdgeDefs(i+1,2) = EdgeDefs(i,2) + 0.5 * (TimeStamp(i+1) -
TimeStamp(i)) * (EdgeVels_f(i,2) + EdgeVels_f(i+1,2));
    EdgeDefs(i+1,3) = EdgeDefs(i,3) + 0.5 * (TimeStamp(i+1) -
TimeStamp(i)) * (EdgeVels_f(i,3) + EdgeVels_f(i+1,3));% + ((7*10^-7) *
(1/Fs)^3) + ((8*10^-5) * (1/Fs)^2) + (0.4787 * (1/Fs));
    EdgeDefs(i+1,4) = EdgeDefs(i,4) + 0.5 * (TimeStamp(i+1) -
TimeStamp(i)) * (EdgeVels_f(i,4) + EdgeVels_f(i+1,4));
    % flap
    FlapDefs(i+1,1) = FlapDefs(i,1) + 0.5 * (TimeStamp(i+1) -
TimeStamp(i)) * (FlapVels_f(i,1) + FlapVels_f(i+1,1));
    FlapDefs(i+1,2) = FlapDefs(i,2) + 0.5 * (TimeStamp(i+1) -
TimeStamp(i)) * (FlapVels_f(i,2) + FlapVels_f(i+1,2));
```

```
    FlapDefs(i+1,3) = FlapDefs(i,3) + 0.5 * (TimeStamp(i+1) -
TimeStamp(i)) * (FlapVels_f(i,3) + FlapVels_f(i+1,3));
    FlapDefs(i+1,4) = FlapDefs(i,4) + 0.5 * (TimeStamp(i+1) -
TimeStamp(i)) * (FlapVels_f(i,4) + FlapVels_f(i+1,4));
End
```

APPENDIX C: TEST PLAN

BLADE FATIGUE TEST PLAN
REV-120718

PHASE-LOCKED EXCITATION (PhLEX) OF A 9-m WIND TURBINE BLADE

DUAL-AXIS RESONANT FATIGUE PROTOTYPE DEMONSTRATION

CONDUCTED BY
National Renewable Energy Laboratory
National Wind Technology Center
1617 Cole Blvd
Golden, CO 80401

CONDUCTED FOR
Embry-Riddle Aeronautical University
600 S. Clyde Morris Blvd
Daytona Beach, FL 32114

18 JULY 2012

APPROVAL BY   _____

          Darris White   Date

          Principal, Embry-Riddle Aeronautical University

APPROVAL BY   _____

          Jenna Beckwith   Date

          Principal, Embry-Riddle Aeronautical University

APPROVAL BY   _____

          Michael Desmond   Date

          Test Engineer, National Renewable Energy Laboratory

APPROVAL BY   _____

          Scott Hughes   Date

          Test Manager, National Renewable Energy Laboratory

TABLE OF CONTENTS

1-CONTACTS

Table 1.1 – Contacts

Name	Title	Email	Phone
NATIONAL RENEWBLE ENERGY LABORATORY			
Dave Simms	Group Manager	david.simms@nrel.gov	303-384-6942
Scott Hughes	Test Manager	scott.hughes@nrel.gov	303-384-7054
Mike Desmond	Engineer	michael.desmond@nrel.gov	303-384-7121
Dave Snowberg	Engineer	david.snowberg@nrel.gov	303-384-6920
Mike Jenks	Technician	mike.jenks@nrel.gov	303-384-6994
Bill Gage	Technician	bill.gage@nrel.gov	303-384-7071
Norman Hill	Technician	norman.hill@nrel.gov	303-384-7120
Mike Stewart	EHS POC	michael.stewart@nrel.gov	303-384-6906
EMBRY-RIDDLE AERONAUTICAL UNIVERSITY			
Darris White	Principal	darris.white@erau.edu	386-226-7036
Jenna Beckwith	Student	jenna.a.beckwith@gmail.com	

2-DISCLAIMER

This test plan shall not be reproduced, except in full, without the written approval of NREL.

3-BACKGROUND

This test will be performed under Subcontract ZEE-9-77584-01, under Prime Contract, DE-AC36-08GO28308, "Analysis and Demonstration of Advanced Dual-Axis Test Methods for Wind Turbine Blades, under NREL Subtask WE110112, Advanced Test Methodology.

The most recent dual-axis testing method, universal resonant excitation (UREX) technology, incorporates multiple flap and lead-lag actuators, each operating at their respective fundamental frequencies, to apply inertial loads onto the wind turbine blade. Although this method is quicker and more efficient than previous testing methods, there is no cycle-to-cycle phase control which could result in undesired application of loads around the blade profile. Therefore, a new technology called phase locked resonance excitation (PhLEX) was developed which will use an additional actuator (spring element) in order to adjust the stiffness of the test article such that the flapwise and edgewise resonance frequencies are equal, allowing control over cycle-to-cycle phase angle. The test will be conducted on the test stand in Building A60 at the NREL. The current PhLEX concept will employ a hydraulic cylinder to adjust the test article stiffness in combination with the UREX for resonant excitation loading.

4-SCOPE

This test plan describes the test setup and defines the load cases and instrumentation during the blade fatigue test. The scope of work considered here includes a full-scale blade fatigue test of a 9-m CX-100 wind turbine blade. Tests will include static calibration pulls, as well as a dynamic dual-axis resonant fatigue test.

This test is being conducted for research and development purposes. However, testing will follow the IEC 61400-23 blade test standard and NREL's Quality Management System where appropriate. Testing will be conducted under NREL's Structural Safe Operating Procedures.

5-OBJECTIVES

The primary objective of the laboratory fatigue test is to demonstrate the PhLEX dual-axis resonant test method. Of importance will be to prove the robustness of the control methodology and the application of cycle-to-cycle load introduction. The objective will not be to damage the blade as a result of testing.

6-TEST ARTICLE DESCRIPTION

The test article will be a 9-m CX-100 wind turbine blade as shown in Figure 6.1. The test article is a structural equivalent of previous Sandia designed CX-100 blades. The test article was fabricated by TPI Composites at their blade production facility located in Warren, Rhode Island. Primary blade construction materials include fiberglass and epoxy with carbon fiber spar caps. Root attachment is through quantity 12 female-threaded 0.75"-16 UNF fasteners equally spaced on a 300-mm bolt circle.
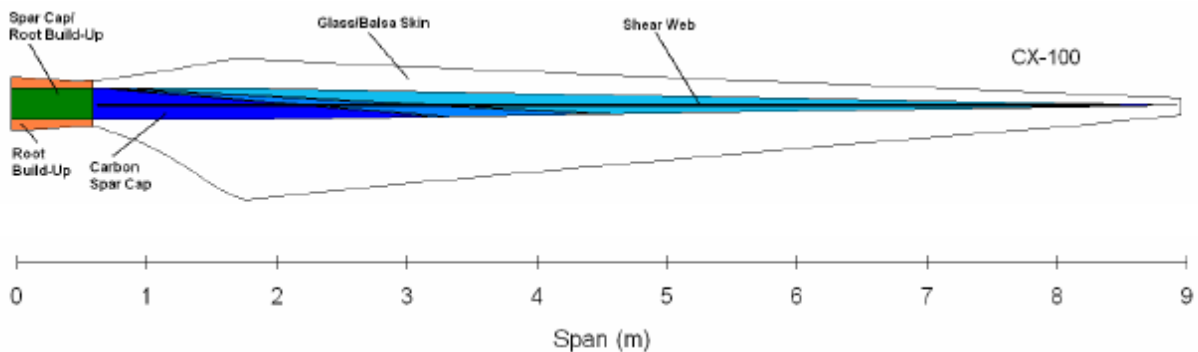
Figure 6.1 – CX-100 9-m Blade

Baseline blade properties were previously provided by SNL, estimated values are presented in Table 6.1. These values are used as inputs to predict system frequencies, operational deflection shapes and applied moments necessary for the definition of a resonant fatigue test.

Table 6.1 – Estimated Blade Properties

Station (%)	Station (m)	MPL (kg/m)	Chord (m)	Flat EI (N-m^2)	Edge EI (N-m^2)	GJ (N-m^2)	Twist (deg)
0.00	0.00	130.42	0.39	2.45E+07	2.45E+07	8.92E+06	29.60
0.02	0.20	130.42	0.38	2.45E+07	2.45E+07	8.92E+06	29.60
0.07	0.60	34.14	0.33	5.39E+06	8.86E+06	2.09E+06	24.80
0.11	1.00	34.73	0.49	4.75E+06	1.23E+07	1.64E+06	20.80
0.16	1.40	32.32	0.77	3.35E+06	1.24E+07	1.43E+06	17.50
0.20	1.80	19.69	1.03	3.01E+06	8.79E+06	8.65E+05	14.70
0.24	2.20	18.13	0.97	2.37E+06	7.69E+06	7.46E+05	12.40
0.36	3.20	15.49	0.83	1.38E+06	4.65E+06	4.23E+05	8.30
0.47	4.20	12.73	0.71	7.04E+05	2.68E+06	2.30E+05	5.80
0.58	5.20	10.26	0.58	3.31E+05	1.40E+06	1.07E+05	4.00
0.69	6.20	7.75	0.46	1.08E+05	6.50E+05	4.48E+04	2.70
0.80	7.20	5.62	0.35	3.11E+04	2.34E+05	1.58E+04	1.40
0.91	8.20	3.27	0.23	4.49E+03	5.42E+04	3.54E+03	0.40
1.00	9.00	2.28	0.12	3.62E+02	6.79E+03	4.97E+02	0.00

The test article has the last 1-meter of the tip section removed. The test article characteristic values are given in Table 6.2. A modal analysis was performed to determine the actual characteristic values of the modified 8 meter blade. Weight and CG measurements will be performed post testing.

Table 6.2 – Characteristic Test Article Properties

Property	Predicted Value 9-m	Predicted Value 8-m	Measured Value 8-m
Blade Weight (kN)	1.60	1.58	n/a
Blade Length (m)	9.00	8.00	8.00
Blade CG (m)	2.24	2.12	n/a
1st Flap Frequency (Hz)	4.30	5.40	5.12
2nd Flap Frequency (Hz)	11.01	16.96	16.18
1st Edge Frequency (Hz)	7.76	9.24	6.82

7-LOADS

7.1-Design Loads
The design loads are based on characteristic fatigue bending moments applied to previous tests of CX-100 blades. These loads were based on a 1-million cycle damage equivalent load and were provided by SNL. The design loads are represented as fully factored test loads for the flapwise direction. The loads are provided for seven spanwise locations as shown in Table 7.1.

Table 7.1 – Target Flapwise Loads

Station (m)	Max (N-m)	Min (N-m)	Range (N-m)	Mean (N-m)
0.00	60770	6080	54690	33420
0.23	62420	6240	56180	34330
1.58	43360	4340	39020	23850
3.38	22950	2290	20660	12620
5.63	7100	710	6390	3910
7.43	1330	130	1200	730
9.00	0	0	0	0

7.2-Test Load Factors
The loads presented are fully factored test loads. No additional test load factors were applied.

7.3-Test Loads
As the loads were presented as fully factored loads, the design loads from Table 7.1 are the target test loads. Note that the moment amplitude about the mean load can be scaled by increasing or decreasing the excitation force (actuator stroke), but the characteristic shape remains essentially unchanged.

The applied bending moment will be measured through calculated strain gage signals. Strain gages are calibrated for bending moment through the application of a single point static load. From the known bending moment and strain measurement, strain versus moment curves are generated, which then allows for moment measurement during the dynamic resonant test. The static calibration loads are applied before the fatigue test and at regular intervals during the fatigue test, as strain sensitivities can change slightly during loading and for cases where gages fail and are replaced.

7.4-Tare Loads
For resonant testing, the tare or mean load is the summation of the moment due to blade weight and moment due the weight of the UREX system components (UREX and ballast weight).

7.5-Operational Deflections
The blade tip deflection peak to peak range is anticipated to be on the order of 0.76-m in the flapwise direction and 0.375-m in the lead-lag direction.

8-TEST SETUP

8.1-Quality and Safe Operating Procedures
All testing will be conducted in accordance with NREL Safe Operating Procedure (SOP) #515009412 – Conducting Structural Tests at the NWTC. An RV will be performed prior to the start of testing. The RV will demonstrate that the test is in compliance with NREL SOP's and all systems are working according to specification.

All NREL staff and visiting professionals shall comply with the SOP and RV while working at the NWTC. Visiting professionals will be required to participate in an NREL EHS orientation before being allowed to participate in testing activities at the NWTC.

Safe Work Permits and Lift Permits will be issued by NREL EHS where work is out of the scope of the structural testing SOP.

8.2-Test Location
The fatigue test will be conducted at NREL at the NWTC on the test stand in Bldg. A-60. The blade will be mounted to the 1,360-kN-m test stand.

8.3-Property Testing
Weight and CG measurements of the blade will be performed with a single point lift prior to installing instrumentation. Simple modal tests will be performed by manually exciting the blade to obtain operational test frequencies via FFT analysis of measured strain gage signals once the blade is mounted to the test stand.

8.4-Facility Configuration
The test stand will be tilted at 4.4-degrees in order to allow the outboard PhLEX actuator to be properly mounted beneath the blade at the 6.75-m station as shown in Figure 8.1.
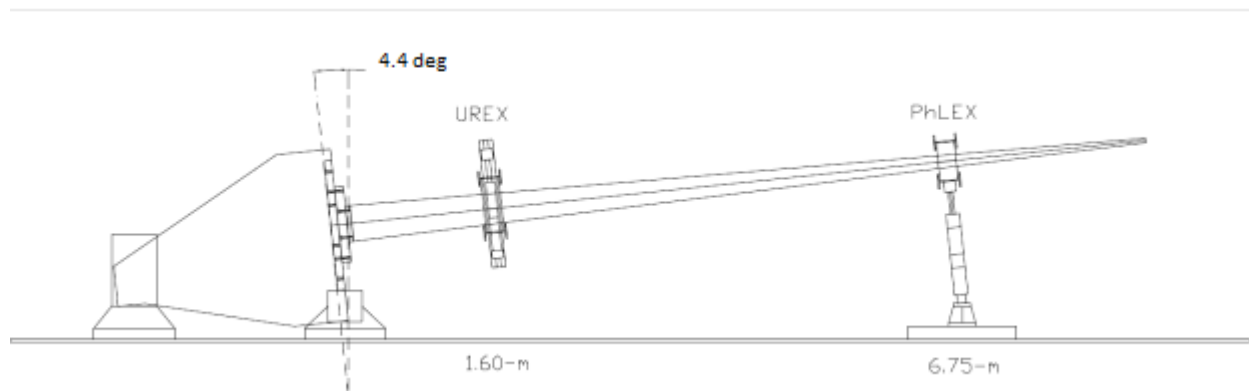
Figure 8.1 – Test Stand Rotation

8.5-Blade Pre-twist Orientation
The blade will be installed in the test fixture such that the HP surface is facing up. The local chord at the 7.0-m station will be rotated to 0-degrees relative to the laboratory floor. To reduce the influence and excitation of higher order modes, the outboard PhLEX actuator will be mounted such that it is angled approximately -1.5 degrees from laboratory vertical.

8.6-Root Fixturing
Twelve 7.0-in long ¾-16 grade 8 fasteners will be used for attaching the blade to the adapter plate. To allow for internal sensor wiring, a custom root shim place is being used. This 2-in thick aluminum shim has slots which allow access to wires inside the blade. The adapter plate is 4-in thick steel and attaches to the test stand using twenty-four 9.0-in long 1-8 grade 8 fasteners, equally spaced on a 30-in bolt circle. Both the shim and adapter plates were used in the previous Sensor and LANL blade tests. Appendix A provides specifications and instructions for mounting the adapter plate to the blade.

8.7-Load Introduction Method

Loads will be introduced to the blade using a resonant loading method, with the blade cantilevered to the test stand.   Oscillating the UREX masses at the system resonant frequency through the integral hydraulic actuators excites the blade, resulting in an alternating bending moment about the mean load. An outboard PhLEX actuator will be used to maintain load phase angle control.

The hydraulic actuators will be controlled with a MTS FlexTest 40 system using displacement control. An accelerometer will be used to control the displacement (through MTS dual-mode control) to compensate for alternating moment fluctuations due to temperature and any blade softening. While the mean test load is indeterminate (mass per unit length of blade is not precisely known a priori), the applied magnitude of the alternating load can be controlled by adjusting the stroke of the UREX actuators, varying the inertial loads applied to the system.

8.8-Load Introduction Hardware
To produce the test loading, the UREX is located at the 1.6-m spanwise station, and a single ballast saddle located at the 6.75-m spanwise station. The weight of the blade, UREX, and ballast saddle provide the mean test load. The PhLEX actuator will be connected to the steel frame of the 6.75-m saddle.

Load saddles will transmit the test loads to the blade. Load saddle forms (wood and rubber) used for this test have been used for previous testing. The load saddle design consists of 6-in thick (in spanwise direction) wood microlams with the airfoil sections cut shaped for each station. A ¼-in to ½-in thick strip of rubber placed between the blade and wood form to protect the blade surface from concentrated point loads. Steel frames are constructed around the wood forms and attach to either the UREX hydraulic system or ballast weights. Saddle installation procedures are provided in Appendix C.

8.9-Controls Strategy
The control system will use MTS 793 software to control actuators mounted to a wind turbine blade for testing. The test will consist of a UREX system to control the blade excitation in the flap and edge directions and a PhLEX system to control stiffness in the flap direction. The addition of the PhLEX actuator requires a dynamic and adaptive control strategy.

The original dual-axis UREX method does not provide cycle-to-cycle control of the applied load phase angle as shown in Figure 8.3.
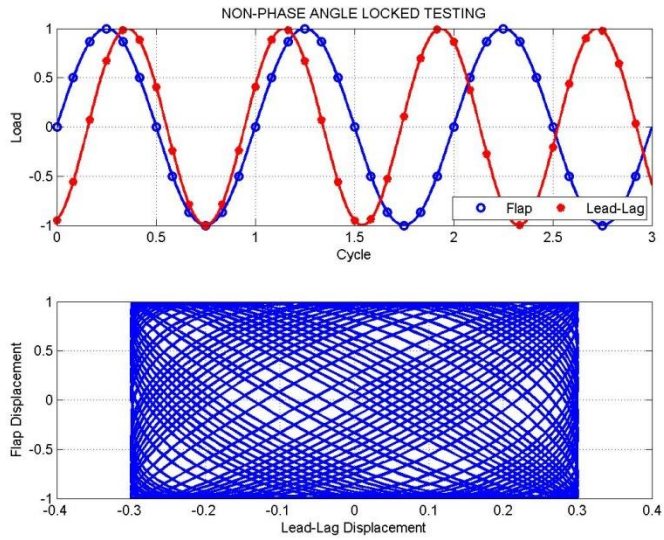
Figure 8.3 – Uncontrolled Phase-Angle Testing

The objective of the PhLEX method is to control the phase-angle relationship and provide constant cycle-to-cycle loading as shown in Figure 8.4.
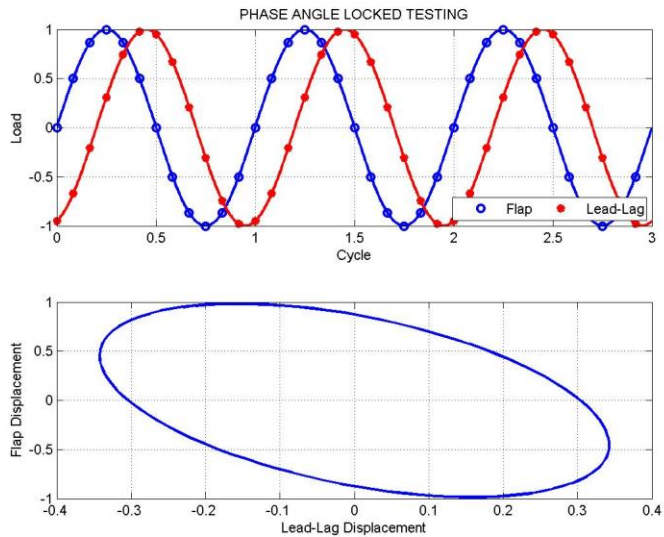
Figure 8.4 – PhLEX Controlled Testing

The inputs and outputs to and from the controller will be in the form of analog and digital signals. The input signals to the controller will come from sensors mounted on the actuators and the blade. The output signals from the controller will go to the actuator controllers. The actuator control signals will be frequency and displacement for the UREX system and force for the PhLEX system. Feedback from the UREX system will be from accelerometer and linear position sensors mounted to the actuator. These signals will validate the intended operation of the UREX system, which is to excite the blade at the natural frequency in both the edge and flap directions. The feedback from the PhLEX system will consist of a load cell placed between the blade and the actuator, an accelerometer sensor, and a linear position sensor. The load cell will

provide feedback on the force exerted by the actuator onto the blade which affects stiffness in the flap direction and will need to be closely and accurately monitored.

The control strategy relies on peak detection to determine phase angle between the flap and edge directions. The current control strategy, modeled in Simulink and based on a simulated blade, detects peaks by watching for the velocity of each direction to go to zero. Once a peak is detected, the phase angle between the edge and flap directions can be determined. The MTS system can detect peaks and, subsequently, phase angle which will both be inputs into the controller.

The control strategy for this blade test has to be able to control four actuators simultaneously to control the phase angle between the edge and flap, which must be maintained at or close to 72°. Peak detection is utilized as a means of finding the phase angle. The calculation of the phase angle consists of finding the percent difference between the times of the peaks of the edge and flap directions. The current phase angle is then filtered to provide a smooth operation of the actuator. The filtered current phase angle is then subtracted from the requested phase angle of 72° to get an error. The error is then run through a PID controller which outputs a force for the PhLEX actuator. This computed force is added to an initial force, which was calculated from the difference in stiffness values between the flap and edge directions, and sent as an analog signal to the PhLEX actuator. Feedback from the PhLEX actuator in the form of a load cell placed between the blade and actuator will let the controller know how much error there is between the requested force and the actual force of the actuator.

The three UREX actuators are controlled by frequency and displacement and both will be set as constant for the entirety of this test. The frequency constant is the natural frequency of the edge and flap, and, since stiffness is being added to the flap direction, these two values are equal. The displacement for the UREX actuators will be calculated using the accelerometer data and the steps shown below, assuming the acceleration (a(t)) is a sinusoidal function and (w) is the natural frequency. Feedback from the UREX actuators in the form of accelerometer sensors will let the controller know if the desired acceleration is being met.

$$a(t) = \sin(wt)$$
$$\int a(t)dt = v(t) = -\frac{1}{w}\cos(wt)$$
$$\int v(t)dt = \Delta x = -\frac{1}{w^2}\sin(wt)$$
$$\Delta x = -\frac{1}{w^2}a(t)$$
$$-w^2\Delta x = a(t)$$

Initial simulations revealed that the blade response was chaotic and noisy as shown in Figure8.5.
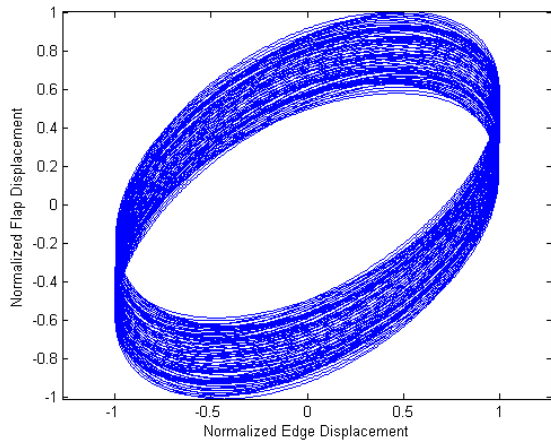
Figure 8.5 – Unfiltered Blade Response

To minimize this, a low-pass pole placement filter was designed and implemented. After the flap and edge natural frequencies were identified, a transfer function containing the edge natural frequency in the numerator and the flap frequency in the denominator. This effectively cancelled the flap frequency and replaced it with the edge frequency, which resulted in a smooth response to any impulse. While this method was effective in smoothing the response of the blade, it increased the force requirement to meet the flap and edge target loads. However, it should be a very robust control method. The filtered blade response is shown in Figure 8.6.
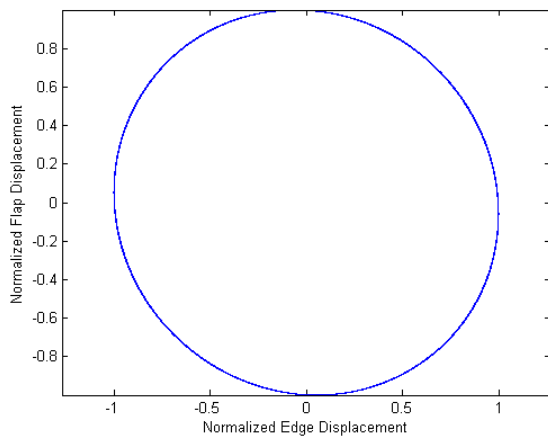
Figure 8.6 – Filtered Blade Response

9-INSTRUMENTATION

9.1-Load
A load cell will be used at the PhLEX actuator to measure loads during the static calibration pulls and during the fatigue test.

9.2-Displacement
The LVDT of the PhLEX actuator will be used to measure deflections during the static calibration pulls and blade stiffness verifications.

Four biaxial DC accelerometers will be used to capture the dynamic blade motion and will serve as the feedback signals for the MTS hydraulic controller.

9.3-Strain Gages
A total of 24 foil strain gages will be installed on the blade for strain measurement and to determine the applied loads based on the calibration pull sensitivities.

There will be 9 strain gage channels around the 3.2-m airfoil profile to capture strain around the airfoil.

9.4-Temperature
Ambient temperature and relative humidity in the vicinity of the blade root will be measured with an Omega sensor.

9.5-Test System Data Acquisition
NREL's Ethercat data acquisition system (EDAS) will be used for this test. Channels will be sampled at 200-Hz, and recorded as peak valley pairs in data files. This data will be recorded continuously throughout the test. Appendix B contains the full channel map.

9.6-Thermography
A Flir SC640 camera may be used as necessary to qualitatively image active thermal regions of the blade.

9.7-Photos and Videos
Still photographs and videos will be taken continuously during test setup and testing.

10-TEST PROCEDURE

10.1-Test Matrix
Table 10.1 provides a representative test matrix showing the load level and number of cycles up to 100% of the target load. For this test, since we are trying to demonstrate the PhLEX test method rather than test the blade, the load level will ramp incrementally in limited cycle block counts. The load level increments will be evaluated and determined based on the response characteristics exhibited by the blade and data collected from the previous load blocks.

Table 10.1 – Test Matrix

Test	Type	Description	% of Target Root Moment Range	Applied Moment (kN-m)	Number of Cycles
1	Static	PhLEX Only	50%	27.35	1
2	Static	PhLEX Only	100%	54.69	1
3	Fatigue	Single-Axis Flap	100%	54.69	5k
4	Fatigue	Single-Axis Edge	100%	17.00	5k
5	Fatigue	Dual-Axis	50%	27.35	5k

6	Fatigue	Dual-Axis	75%	41.02	5k
7	Fatigue	Dual-Axis	100%	54.69	5k
8	Fatigue	Dual-Axis PhLEX	25%	13.67	5k
9	Fatigue	Dual-Axis PhLEX	50%	27.35	5k
10	Fatigue	Dual-Axis PhLEX	75%	41.02	5k
11	Fatigue	Dual-Axis PhLEX	100%	54.69	5k

10.2-Fatigue Test Procedure
The test sequence is provided as follows:
Perform basic modal test.
Perform static calibration pulls.
Perform fatigue test shakedowns.
Enable and demonstrate test controls and interlocks.
Compare with target loads.
Adjust ballast if needed.
Adjust amplitude as needed.
Collect signatures and distribute test plan.
Perform Readiness Verification.
Management and EHS authorization required for unattended operation.
Run test for each load block identified in Table 10.1.
Enable and demonstrate test controls and interlocks.
Daily inspection of hydraulic system.
Daily physical inspection of blade.
Daily inspection and review of data.
Replace/repair strain gages as necessary and calibrate as needed.

10.3-Property Testing
Weight and CG measurements along with a basic modal test of the blade will be conducted prior to the beginning of the fatigue test.

10.4-Static Calibration Pulls and Stiffness Checks
Before testing begins, a static calibration pull will be conducted in the positive flapwise direction using the PhLEX actuator. During these calibration pulls, strain versus applied bending moment values will be derived for use in the resonant test, based on strain gage and load cell readings. The target load level is 2.3-kN which will be applied at the 6.75-m saddle. This will apply a root bending moment of approximately 28% of the target root fatigue test range moment. Expected tip deflection in the flapwise direction is 0.15-m.

11-REPORTING

NREL will provide a summary letter report covering system operation and blade test system DAS for the test 30 working days after the completion (removal from facility) of the test. This report will not cover any details on any of the other test partner systems.

12-EXCEPTIONS FROM STANDARD PRACTICE

Exceptions from standard practice as of the current test plan revision:
None.

13-UNRESOLVED ISSUES

Unresolved issues as of the current revision of this test plan:
None.

14-REFERENCES

"Structural Testing of 9 m Carbon Fiber Wind Turbine Research Blades" J. Paquette, J. van Dam, S. Hughes, 45th AIAA Aerospace Sciences Meeting and Exhibit, Reno, Nevada, January 2007, http://www.sandia.gov/wind/asme/AIAA-2007-Testing9m.pdf.
"Modeling and Testing of 9m Research Blades" J. Paquette, D.L. Laird, D.T. Griffith, L. Rip 44th AIAA Aerospace Sciences Meeting and Exhibit, Reno, Nevada, January 2006, http://www.sandia.gov/wind/asme/AIAA-2006-Modeling9m.pdf.

APPENDIX A-Test Hardware and Blade Installation Procedures

Adapter Plate Installation – The following steps shall be followed for attaching the blade to the adapter plate.
Clean adapter plate mounting surface, test stand face, and blade root studs with wire brush, then cloth towel to remove any debris.
Ensure Blade is clocked correctly with reference to the adapter plate.
Ensure capscrews are Grade 8 (fully hardened washers).
Attach bolts through adapter plate, shim and spacer assembly
Lubricate Threads with moly-based anti-seize.
Torque all capscrews to 20 ft-lb.
Torque to 100 ft-lb in a star pattern.
Torque to 287 ft-lb, in a star pattern.
Check torque at 287 ft-lb in a circular pattern.

Blade Mounting – Following table provides +-2% lift weights for mounting to the test stand.

	Local CG [in]	CG from stand Face [in]	Weight [lb]	CG*W		
Blade	90.8	96.8	386	37364.8	CG from stand [in]	28.1
Adapter	2	2	950	1900	**CG from root face [in]**	**22.1**
Shim	1	5	69	345	**Total Lift Weight [lb]**	**1411**
Bolts	3.5	3.5	6	21		
		sums	1411	39630.8		

The following steps shall be followed for attaching the blade and adapter plate to the test stand
Using a 5000-lb min choke sling, choke blade at CG while avoiding sensors on blade.
Lift and angle blade with overhead crane to mount flush with face of stand, ensure clocking of blade correct.
Torque in a star pattern the (24) Grade 8 adapter to stand fasteners to 550 ft-lb lubed.
Relax load on crane.

Saddle Attachment – Following steps shall be followed to attach saddles to blade
Position saddle at correct spanwise station
Ensure saddle is square to pitch axis of blade
On alternating corners, tighten allthread to 40 ft-lb.
Check that saddle does not pivot in any direction on the blade

APPENDIX B- NREL EDAS Channel Map

Channel	Name	Type	Location (mm)	Surface
1	SG0500HP00SC	Strain Gage	500	HP
2	SG0500LP00SC	Strain Gage	500	LP
3	SG1400HP00LE	Strain Gage	1400	HP
4	SG1400HP00SC	Strain Gage	1400	HP
5	SG1400HP00TE	Strain Gage	1400	HP
6	SG1400LP00SC	Strain Gage	1400	LP
7	SG2000HP00SC	Strain Gage	2000	HP
8	SG3500HP00SC	Strain Gage	3500	HP
9	SG3500LP00SC	Strain Gage	3500	LP
10	SG5000HP00LE	Strain Gage	5000	HP
11	SG5000HP00SC	Strain Gage	5000	HP
12	SG5000LP00SC	Strain Gage	5000	LP
13	SG6500HP00SC	Strain Gage	6500	HP
14	SG6500LP00SC	Strain Gage	6500	LP
15	SG7000HP00SC	Strain Gage	7000	HP
16	SG3600HP10TE	Strain Gage	3200	HP
17	SG3600HP20TE	Strain Gage	3200	HP
18	SG3600HP28TE	Strain Gage	3200	HP
19	SG3600HP36TE	Strain Gage	3200	HP
20	SG3600LP04TE	Strain Gage	3200	LP
21	SG3600LP11TE	Strain Gage	3200	LP
22	SG3600LP18TE	Strain Gage	3200	LP
23	LVDT-N	Displacement	1600	North UREX Actuator
24	LVDT-S	Displacement	1600	South UREX Actuator
25	LVDT-E	Displacement	1600	Edge Actuator
26	LVDT-P	Displacement	6750	PhLEX Actuator
27	LC-P	Load	6750	PhLEX Actuator
28	TEMP	Temperature	0	Ambient
29	HUM	Humidity	0	Ambient
30	AC1700Flap	Accelerometer	1700	HP
31	AC1700Edge	Accelerometer	1700	HP
32	AC2500Flap	Accelerometer	2500	HP
33	AC2500Edge	Accelerometer	2500	HP
34	AC6650Flap	Accelerometer	6650	HP
35	AC6650Edge	Accelerometer	6650	HP
36	AC8000Flap	Accelerometer	8000	HP
37	AC8000Edge	Accelerometer	8000	HP

APPENDIX C- Predicted Strain in Blade

The strain distribution shown in the following figures was obtained by matching the blade to a displacement curve. The displacement curve was determined by matching the displacement of the blade to the manufacturer specified moments along the blade. The maximum strain in the edgewise direction was found to be 7e-04. The maximum strain in the edgewise direction was found to be 2e-03.
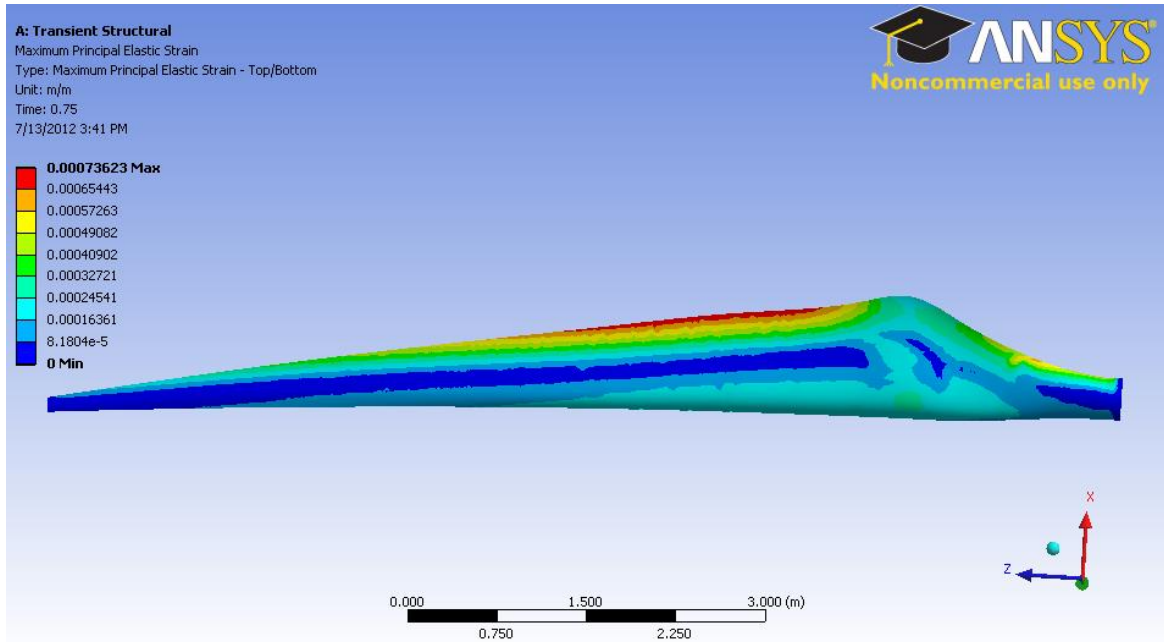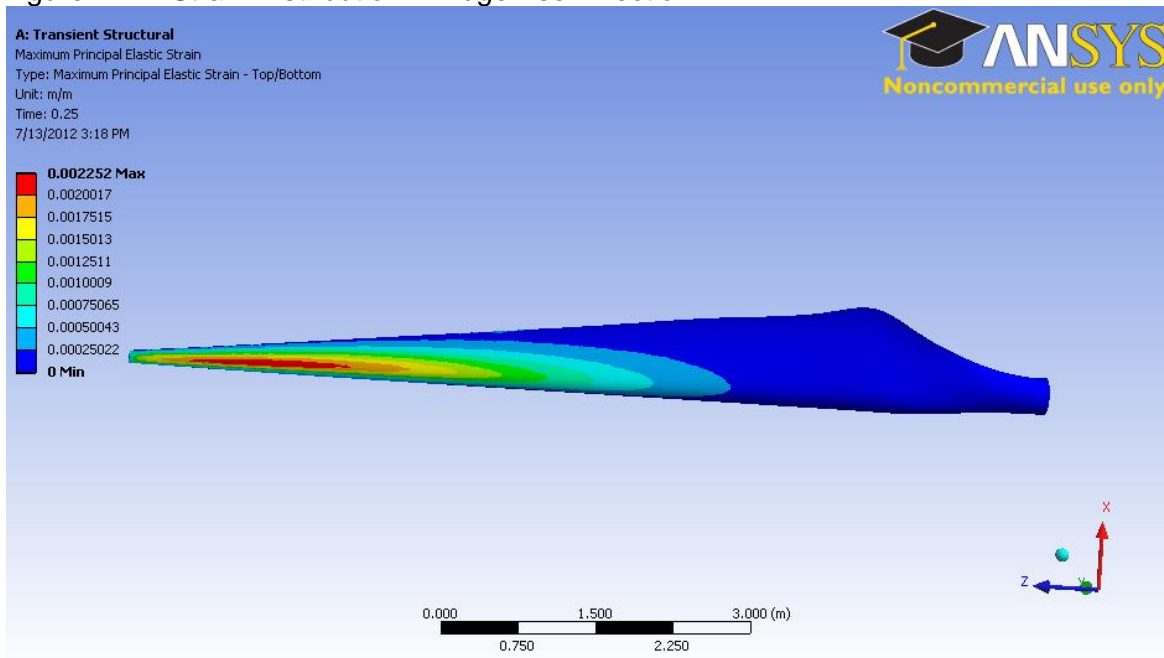

Figure A.1 – Strain Distribution in Edgewise Direction

Figure A.2 – Strain Distribution in Flapwise Direction